Utrecht University

Faculty of Geosciences

Studying landslide deformations using Remote Sensing and field surveys

A raster and point cloud approach for the Charonnier landslide, France

A thesis submitted in partial fulfilment of the requirements for

Master's degree in Earth Surface and Water

Author:

Itsaso Guembe Cia

i.guembecia@students.uu.nl

Supervisors:

Prof. dr. Steven de Jong

Dr. Rens van Beek

Utrecht

July 2018

Abstract

Landslides are among the most widespread hazards in the word, with special relevance in mountainous regions. In January 1994, a rainfall-triggered rotational landslide mobilised about 28000m^3 of material from the hillslopes of the Charonnier basin, in the French department of Hautes-Alpes. Hydrological and geotechnical surveys are classic approaches for stability studies, built upon in situ observation and soil parameterization. Nevertheless, the introduction of remote sensing systems for landslide mapping and monitoring in the last decades yields intersecting results, yet their possibilities are not fully exploited and remains nowadays a promising area of study. Reconstruction of landslide topography and its evolution throughout the years is achievable with the help of photogrammetry techniques. In the present study, historical aerial pictures from 1993 and 1999 are used to generate elevation information of the Charonnier landslide area in raster (DTM) and point cloud (DPC) format. Resolution of the available historical photographs appears to be a crucial factor for the accuracy of the derived products, decreasing their RMSE from 3.4m to 0.14m (900dpi vs. 2400dpi images). With the help of a UAV, which captures on demand, high-resolution images, elevation models for 2016 and 2017 are built with errors around 10cm.

1993, 1999, 2016 and 2017 products are compared to distinguish morphodynamic processes in the short and long term. DTMs corresponding to different dates are subtracted one from the other, to detect areas where terrain elevation has varied. This way, the location of the source area and volume of the displaced mass are drowned. The distance between DPCs for different dates is computed with the M3C2 algorithm. The main outcome of the computation is the delimitation of areas subjected to erosion in the flanks of the Charonnier creek, in the form of gullies, and of riverbed incision of around 10cm/year.

A soil sampling campaign and material characterization were carried out in June 2017. Soil characteristics, like dry bulk density or porosity, do not show significant spatial or temporal variability when compared to 2016 results.

Acknowledgments

I would like to thank my supervisors from Utrecht University, Prof. Dr. Steven de Jong and Dr. Rens van Beek for their support and encouragement during the development of this research. Their ideas and feedback were very helpful for defining the focus of this study. I also acknowledge the help that Dr. Maarten Zeylmans Van Emmichoven offered to me in the processing of the historical aerial pictures, and Henk Markies for operating the UAV during the field campaign. Lastly, I greatly appreciate the love and inspiration that my friends and fellow students in Utrecht gave to me last months.

Contents

1. Introduction 7
2. Theoretical background of landslides and remote sensing 11
2.1 Morphology of landslides 12
2.2 Stability of landslides 12
2.3 Remote Sensing applied on the study of landslides 15
3. Research area condition 18
3.1 Geology and geomorphology 18
3.2 Meteorology 19
3.3 The 1994 event 20
4. Methods & Data 21
4.1 Remote sensing and photogrammetry 21
4.2 Soil characterization 29
5. Results 33
5.1 Landslide dynamics and remote sensing 33
5.2 Soil characteristics 43
6. Discussion 45
6.1 Remote sensing, photogrammetry and GIS 45
6.2 Soil characterization 46
7. Conclusions 47
7.1 Research questions 47
7.2 Recommendations 48
8. References 49
9. Appendix 53

1. Introduction

Landslides are recognized as the third type of natural disaster in terms of worldwide importance, and pose a major hazard in steep areas located in hilly mountainous regions, river banks and coastal zones (Ayala & Ferrer, 1989; Dikau et al., 1996; Guzzetti, 2000a; Kjekstad & Highland, 2009; Schuster & Fleming, 1986). Intense rainfall events, earthquakes and changes in land use are the main triggering factors, which affect the stability of the slopes, resulting in the downward and outward movement of slope-forming materials (Varnes & International Association of Engineering Geology (IAEG), 1984) (See figure 1.1 for a case in 2010).

The International Disaster Database, EM-DAT (Guha-Sapir, 2017) reports 284 landslides between 2001 and 2016 globally, resulting in more than 13000 casualties, 95.8% of them in Asia. Economic damage is estimated roughly below USD 3 billion (Table 1.1).

Figure 1.1 Landslide in Wangong village, China, in July 2010. Heavy rains caused floods, bridge collapses and landslides, leaving nearly 1000 people dead.

Landslides data aggregated by year shows 2010 as the worst year in the period in terms of casualties (3427) and economic damage (USD 1.3 billion) after 32 events (Figure 1.2). 13 landslide episodes were accounted in 2016, usually led by earthquakes, hurricanes and severe storms, causing estimated economic losses of USD 725 million and 361 casualties (Guha-Sapir, 2017) . The Swiss Reinsurance annual catastrophe report (Swiss Re, 2017) shows slighly different data for 2016: more than 15 episodes than caussed estimated losses of USD 400 million.

Table 1.1 Human and economic impact of landslides between 2001 and 2016, aggregated by continent. Data from The International Disaster Database EM-DAT (Guha-Sapir, 2017).

Continent	Events count		Casualties		People affected		Damage (USD million)	
	Absolute	%	Absolute	%	Absolute	%	Absolute	%
Africa	22	7,7	739	5,5	47490	1,1	0	0,0
America	53	18,7	2072	15,4	113392	2,7	896	29,9
Asia	197	69,4	10371	76,8	3959242	95,8	1919,8	64,1
Europe	5	1,8	172	1,3	441	0,0	180	6,0
Oceania	7	2,5	143	1,1	11095	0,3	0	0,0
Total	284		13497		4131660		2995,8	

As a result of climate change, the frequency of some extreme rainfall events is expected to increase. Additionally, the decay of glaciers and the degradation of permafrost due to more frequent extreme warm temperatures can affect slope stability in high-mountain areas. High temperatures enhance the production of water by melt of snow and ice, and reduce slope strength (Huggel et al., 2010). Population growth and the rise of economic activities has led to the occupancy of new lands, sometimes prone to mass wasting processes, making society more vulnerable to this type of hazard (Castellanos Abella, 2008; Hearn & Hart, 2011).

The understanding of landslides processes needs to be improved in order to reduce the damage and number of casualties resulting from these phenomena presently and in the future. Identifying the trigger mechanisms, developing methods for landslide susceptibility mapping, keeping historical records of landslides and developing flexible and reliable monitoring methods appear as major research fields. In many occasions, physically based models play an important role when these objectives are addressed and require accurate input data in order to obtain valuable results. The characterization of the material involved in the landslide is crucial to understand the hydrological and mechanical properties of the slope and it spatial and temporal variability, and is employed to determine the parameters adopted in such models (Cammeraat et al., 2001; Caris & Van Asch, 1991; Malet et al., 2005).

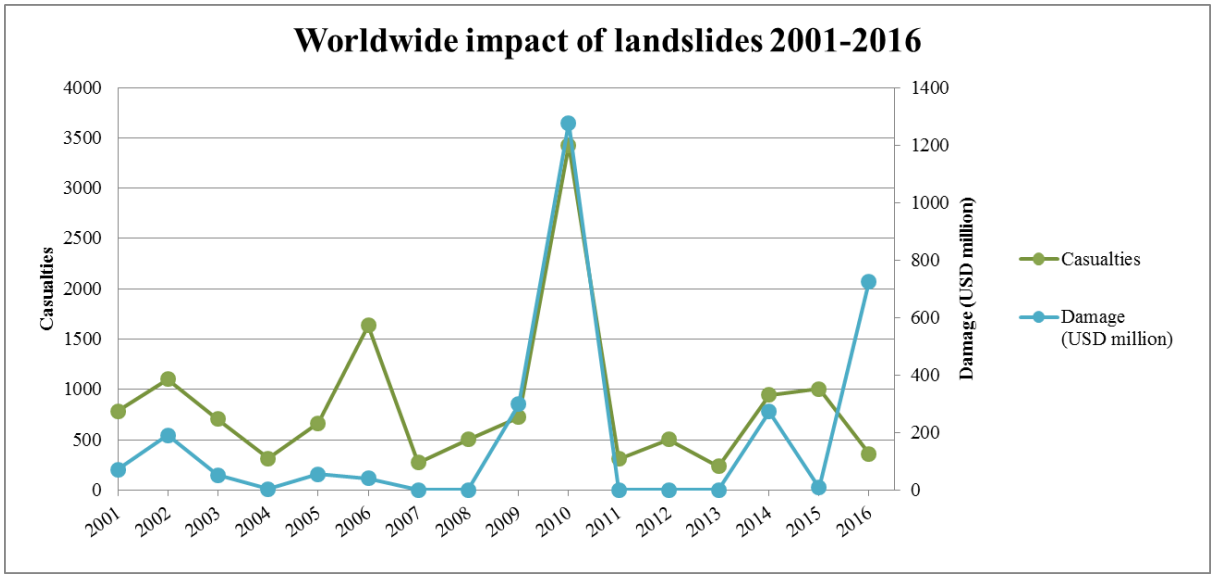

Figure 1.2 Casualties and economic damage caused by landslides worldwide between 2001 and 2016. Data from The International Disaster Database EM-DAT (Guha-Sapir, 2017).

The development of mapping and monitoring methods appears as a research area which can yield interesting results (Lucieer et al., 2014; Turner et al., 2015). During the last decade, there has been an increase in the use of remote sensing technology for both purposes. Still, this technique is not fully exploited, and only since the beginning of the 2000s stereoscopic air-photo interpretation has been replaced or combined with other techniques (Metternicht et al., 2005; Turner et al., 2015); there has been a significant improvement in the spatial resolution of remote sensing technology with the introduction of laser scanning (both airborne and terrestrial) and unmanned aerial vehicles (UAVs).

A frequent application of this technology is the creation of digital elevation models (DEM), which can be included in landslide modelling as topographical information. Time series of DEM, in raster format, and elevation information in point cloud format, can also be compared by different means in order to detect and monitor changes in the morphology of the landslide under study. The computation of distances between two point clouds is a newly developed technique with great advantages when comparing topography of very steep areas (Busker, 2017; Cook & L., 2017; Lague et al., 2013).

In the French department of Hautes-Alpes, in Southern France, an extremely wet period between September 1993 and February 1994 caused the failure of hundreds of hillslopes (Pech & Sevestre, 1994), emphasizing the importance of this kind of hazard in this area and causing serious disruptions on populated areas, infrastructures and agricultural lands. Several explorations conducted in the area have shed light on the local conditions that triggered and drove these mass wasting process, based on geological and geotechnical properties of the local material. In areas under Mediterranean climate conditions, landslides are closely related to intense rainfall events and changes in hydrogeology (Ayala & Ferrer, 1989; T. Bogaard, 2001; Guzzetti, 2000b; Van Asch et al., 2007).

This study explores the applicability of the remote sensing and soil characterization approaches to detect geomorphological processes. A case study carried out on a small landslide that initiated on 7th January 1994 near the Charonnier River, in the Büech basin in the Hautes-Alpes region. Historical aerial photographs taken before and after the event and UAV based imagery collected in June 2017 are used for the production of DTMs and dense point clouds, which together with elevation models from June 2016 by De Vries (2017) and Van Haaster (2017) and soil samples (from field campaigns in June 2016 and June 2017) are included in the assessment of the long-term and short-term dynamics of the landslide. These objectives are addressed in this document with the help of the following research questions:

1. Can dynamics since 1993, before the landslide event, be determined with the help of coarse historical aerial photographs acquired at different dates?

2. Has the landslide been subjected to any motion between 2016 and 2017? Is there any other secondary process modifying the morphology of the landslide?

3. Can a comparison between 2016 and 2017 very high-resolution UAV based photogrammetry products give information about which kind of geomorphological processes are acting on the landslide area in the short term?

4. Can both, a differential DEM and a cloud to cloud distance calculation, yield meaningful information about topographical changes for both timescales?

5. Can temporal variability of soil properties be determined upon very limited sampling campaigns?

The following chapter introduces theoretical background on landslides and remote sensing. Chapter 3 gives an overview of the local conditions around the Charonnier landslide, followed in the next section by an explanation of the applied methods and data. Chapter 5 compiles the results of this study, which are discussed in chapter 6. Conclusions in relation to the proposed research questions and their applicability to other study areas, together with some recommendations will be approached in the last chapter.

2. Theoretical background of landslides and remote sensing

Landslides are mass movements characterized by the rapid movement of the material, which suffers little or absent internal deformation. Rupture occurs on one or more surfaces, which are usually associated with discontinuities in bedded or foliated rocks, cemented soil horizons or bedrock interface (Embleton and Thornes, 1979; USGS, 2004). In the case of rotational landslides, the surface of rupture is curved concavely upward and the slide movement is roughly rotational about an axis that is parallel to the ground surface and transverse across the slide. Otherwise, in translational landslides, mass moves along a roughly planar surface with little rotation (Varnes, 1978). Initiation of this kind of slope movements is frequently related to high rainfall events that saturate the material or prolonged weathering processes which reduce the strength of the material. Often, another phase follows the first movement, in which the toe area may deform in a complex way: the ground may bulge, the slide may creep or even flow, possibly over existing failures (Varnes, 1978).

Terms "landslide" and "mass movements" or "mass wasting" have been used indistinctly to name all varieties of slope movements, including some that involve little or no true sliding. However, in the last decades, in order to increase the precision in technical communication, it has been widely accepted the use of "landslide" to describe a specific type of slope movement, while "mass movements" and "mass wasting" can be considered synonyms and describe, more broadly, processes that result in the downward and outward movement of slope-forming materials including rock, soil, artificial fill, or a combination of these (Varnes, 1978).
The EPOCH 1993 project (Casale et al., 1993) classified mass movements based on the causes, movements and material type, and distinguishes 8 types, shown in table 2.1: falls, topples, lateral spreading, rotational or planar landslide, flow and complex movements.

Table 2.1 Type of mass movements following the EPOCH 1993 classification and material involved.

Type of movement	Type of material		
	Rock	Debris	Soil
Fall	Rock fall	Debris fall	Soil fall
Topple	Rock topple	Debris topple	Soil topple
Lateral spreading	Rock spreading	Debris spreading	Soil spreading
Rotational landslide	Single/multiple/successive		
Planar landslide	Block or rock slide	Debris slide	Slab or mud slide
Flow	Sackung or rock flow	Debris flow	Soil flow
Complex movements	e.g. Rock avalanche	e.g. Flow slide	e.g. Slump or earth flow

2.1 Morphology of landslides

Landslides usually present distinguishable morphological features. The study of those elements (Figure 2.1) gives information about the mass movement process and it can be useful to predict further activity (Metternicht et al., 2005).

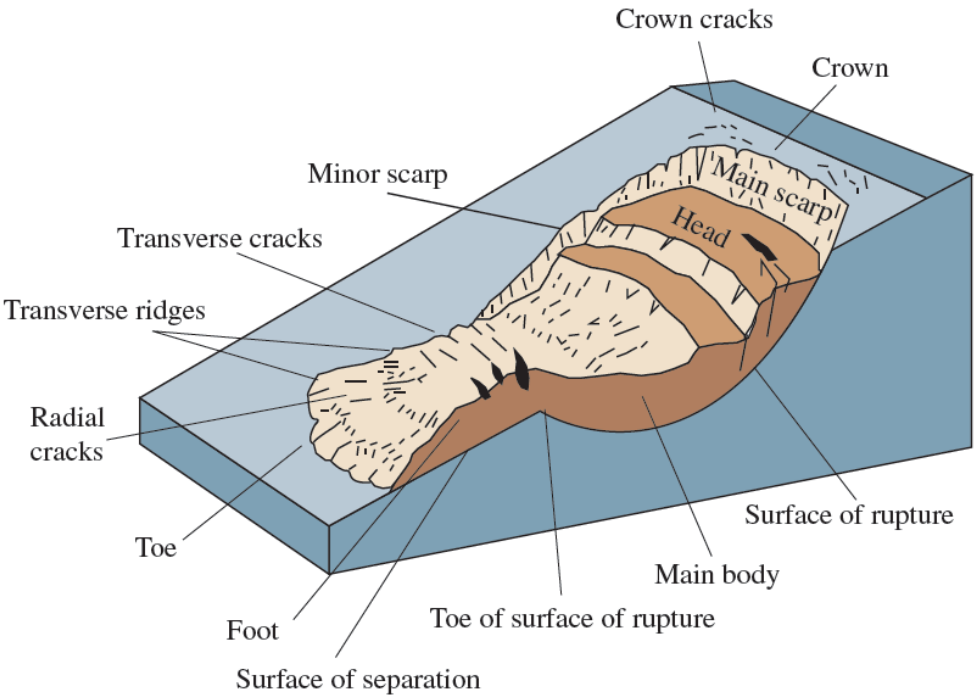

Figure 2.1 Morphological features in a rotational landslide (USGS, 2004)

The material that remains undisturbed and in place delimits the crown, that is located in the top part of the main scarp, which is a steep surface on the undisturbed material at the upper edge of the landslide. This is caused by the movement of the displaced material away from the undisturbed ground and where the parent material is exposed. The head is the upper part of the landslide along the contact between the displaced material and the main scarp. The surface of rupture is the boundary between the original ground surface and the displaced material that has slid on it. Cracks in the foot and toe can indicate activity and its velocity (Cruden & Varnes, 1996).

2.2 Stability of landslides

Landslides are the manifestation of the inertia of the landscape to adapt to changes in the intrinsic or extrinsic factors that affect slope stability (van Beek, 2003). A hillslope fails when forces or stresses acting upon it overcome the strength of the earth materials. Some of the forces acting on a hillslope are gravity, pore-water pressure, tectonic uplift, and earthquake shaking. Geologic composition and stress state, determine the strength of slope material and is modified by past movement, weathering, vegetation, and hydrologic processes (Lu & Godt, 2013).

The safety factor (FoS) assesses the stability of a slope against failure, and is described as the ratio of resistance force to disturbing force. When stress forces become greater than resistance shear forces and FoS becomes smaller than 1, the slope material moves (See figure 2.2).

$$\text{FoS} = \frac{\text{Shear strength}}{\text{Shear stress}} \quad (1)$$

2.2.1 Forces acting in a landslide

Slope stability analysis requires the modelling of how soil transmits internal stresses and deforms under the action of forces. Following Skempton & Delory (1957) approximation for a flat slipping surface, forces acting on the surface of rupture can be estimated upon characteristics of the material involved.

- Shear stress τ is the result of applying a force to the cross sectional area and is a component with direction down the shear plane. It is related to the inclination of the slope (α) and saturated density of the material (γ):

$$\tau = \gamma\, z\, sin\, \alpha\, cos\, \alpha \quad (2)$$

where z is the depth of the failure surface below the ground surface.

- The effective normal stress (σ') that acts perpendicular to the mass body. σ on the slip surface is

$$\sigma' = (\gamma - m\,\gamma_w)\, z\, \cos^2 \alpha \quad (3)$$

where γ_w is the density of water and m is the depth of groundwater above the slip surface.

- Shear strength is the sum of forces resisting downward movements: friction and cohesion (Bogaard, 2001). Effective cohesion (c') is the resisting force per unit area as a result of particle bounds in the material. The frictional resistance is dependent to the area of contact and the mass of the body, and is related to the maximum angle to which a material can be exposed without failure, determined by the angle of internal friction of the soil (ϕ') (Embleton and Thornes, 1979). Both parameters can be determined via a direct shear test (Selby, 1993). Shear strength on the slip surface is

$$s = c' + (y - m\,Yw)\, z\, cos^2\, \alpha\, tan\, \phi' \quad (4)$$

FoS can be described then as

$$FoS = \frac{c\prime}{\gamma\, z\, sin\, \alpha\, cos\, \alpha} + \frac{tan\, \phi\prime}{tan\, \alpha} - m\, \left(\frac{\gamma_w\, tan\, \phi\prime}{\gamma\, tan\, \alpha}\right) \quad (5)$$

- The pressure of water (u) in the pores strongly affects the equilibrium of forces in a soil; the coexistence of fluid and solid phases in a soil is the principle of effective stress (σ'). Stresses imposed on a soil mass are borne by its structure and grain-to-grain contacts (Embleton and Thornes, 1979). Only a part of the total internal stress, the effective stress (σ), is actually transmitted to the soil skeleton and is responsible for its deformation, as the other part is supported by incompressible water (Bogaard & Greco, 2016)

$$\sigma = \sigma' + u. \quad (6)$$

Each of the in- and outward fluxes of water (i.e. infiltration, runoff) affect the groundwater table, which in its turn determines the saturation of the soil, the cohesion and the pore water pressure (Selby, 1993; Van Asch et al., 2009). Above the groundwater table pore pressures are negative; below the groundwater table the pore pressure is positive.

Hydraulic properties, such as conductivity, porosity and permeability, are then relevant when the fluxes of groundwater and the rate at which they flow in saturated systems are taken into account. According to Darcy's low, this flow (Q, m^3/s) depends on the hydraulic conductivity of the soil (K, m/d) and the existence of a matric potential (Ψ, kPa):

$$Q = \frac{-K\,A\,(\Delta\Psi)}{\Delta Z}, \quad (7)$$

where ΔZ is the distance (m) over which the pressure drop takes place.

In unsaturated soils characterized by the absence of a hydraulic gradient, large macro-pores are present, while water fills small pores. Soil properties such as dry bulk density, porosity and hydraulic conductivity determine how much water will infiltrate from the surface to the unsaturated zone and how much will cause overland flow and thus erosion, becoming substantial indicators for the infiltration characteristics that affect the slope stability. The total porosity influences the amount of water that can be stored in a soil. Porosity depends on particle size, compaction and pore distribution. Fissures and cracks can lead to preferential flows and rapid infiltration, altering the permeability and conductivity of the soil.

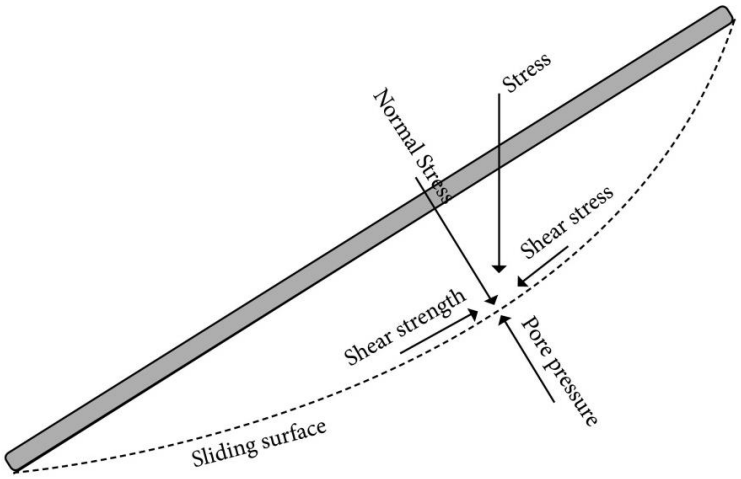

Figure 2.2. Forces acting in a landslide (from de Vries). Frictional and cohesive forces (shear strength) counteract gravity forces (shear stress). Pore pressure supports part of the normal stress imposed to the soil mass.

2.2.2 Causes

Intrinsic and extrinsic factors can cause the development of slope movements. The first ones are related to the reduction of friction forces and influence the stress distribution above the potential slip fault and can be caused by an increase in pore water pressure or decreasing of material strength properties (e.g. weathering of the rock). Extrinsic factors influence the stress distribution indirectly by increasing the gravity force (e.g. by an undercutting of the slope) (T. Bogaard, 2001; Lu & Godt, 2013; van Beek, 2003).

The difference between a cause and a trigger is the time scale over which the processes take place. Intrinsic factors often change gradually over time, while extrinsic factors change rapidly and can be regarded as triggering factors.

Mass movement causes are then related to internal processes (Embleton and Thornes, 1979):

- Weathering reduces the cohesion of the material in the slope by the action of water, air or chemicals. It can also affect the water table and pore pressure and leads to the formation of regolith (T. Bogaard, 2001; Embleton and Thornes, 1979).

- Progressive fissuring, lateral expansion and strain softening of materials, as well as thaw-freeze cycles, can decrease the shear strength of the soil.

- Water percolation through cracks and joints can affect the surface tension of saturated soils and the water pore pressure.

2.2.3 Triggering factors

Trigger can be defined as an external stimulus that causes a near immediate response in the form of a landslide by rapidly increasing the stress or by reducing the strength of slope materials (Wieczorek, 1996), which makes the safety factor of the slope taking values smaller than 1. The requisite short time frame of cause and effect is the element that identifies a landslide trigger.

Earthquakes, which lead to a reduction of normal stress; intense rainfall events, which increase pore water pressure; sudden decrease of groundwater level due to pumping leading to cracks and fissure and affecting the material structure and strength; loading of material increasing shear stress; and unloading of material reducing strength are all processes that can trigger a mass movement (Embleton and Thornes, 1979; Van Asch et al., 2009; D. J. Varnes, 1978).

2.3 Remote Sensing applied on the study of landslides

Remote sensing can be defined as the acquisition and recording of information about an object without being in direct contact with that object (Gibson & Power, 2000). To do so, reflected or emitted electromagnetic radiation has to be registered by a sensor (Legg, 1994). Following this definition, the first photographic camera developed by Nièpce and Daguerre in 1839 can be considered the first sensor capable of storing information in form of an image by means of a photographic emulsion (Konecny, 2003). The term “remote sensing” is restricted, in the field of the geosciences, to the acquisition of information, usually in image form, about the surface of the land masses and oceans, and the atmosphere above it, by airborne or spaceborne sensors. Every remote sensing system includes four components: a source of electromagnetic energy (sun’s reflected energy, earth’s emitted heat or a man-made source as microwave radar); the atmospheric interaction with the energy passing through it, which becomes distorted, absorbed or scattered; the earth’s surface interaction with the electromagnetic energy, characterized by the

objects at the surface, determines the intensity and aspect of the reflected electromagnetic radiation; and the sensor, which register emitted or reflected electromagnetic energy, and can be passive (using the sun or the earth as energy source) or active (emitting electromagnetic energy itself).

The electromagnetic spectrum is the range of all types of electromagnetic radiation, with different wavelengths and energy. Sensors applied in remote sensing can detect wavelengths from 0.2μm to 10^6μm (1m). Their spatial and spectral resolution show great variability, which delimits their applicability. Nowadays, remote sensing applications go from meteorological observation to mining, crop monitoring, biomass calculation, civil protection or natural disaster's damage evaluation (De Jong et al., 2015).

Research on mapping and monitoring of landslides has incorporated the use of earth observation technologies during the last decade. However, this technique is not fully exploited, and only since the beginning of the 2000s stereoscopic air-photo interpretation has been replaced or combined with other remote sensing techniques (Metternicht et al., 2005; Turner et al., 2015); there has been a significant improvement in their spatial resolution with the introduction of laser scanning (both airborne and terrestrial) and unmanned aerial vehicles (UAVs).

Remote sensing technology is useful to produce sets of digital elevation models (DEMs), orthophotos and images with a high temporal and spatial resolution. The understanding of landslide dynamics as flow and expansion rates, volume of accumulated material, scarp retreatment and other topographical changes has significantly benefited from the availability of these products (Lucieer et al., 2014).

UAVs can be related as the most flexible remote sensing platform. Spaceborne and airborne image acquisitions require thorough planning and might be hampered by unfavourable weather conditions. However, UAV technology provides high-resolution outcomes, being able to carry diverse sensors and flying on-demand.

The advance on UAV technology has occurred at the same time of the advance on photogrammetry techniques. Structure from Motion (SfM) algorithms allow the creation of 3D models from sets of overlapping images, and can be applied at diverse scales (form small architectural objects to vast mountainous areas as glaciers in the Himalayas (Immerzeel et al., 2014)).

SfM uses the displacement between different images to extract the relief of the observed area; the same object is displayed at different heights and angles related to each photograph. With this approach, camera position is retrieved from the identification in the image of ground control points (GCP) with known coordinates.

The present document focusses on the detection of small-scale topographical changes. Along with UAV sensors, diverse remote sensing tools have been used in the geomorphology field and, most specifically, in landslide monitoring. Temporal and spatial resolution has to be sufficient in order to detect the modifications, which can be interpreted and provide information about displacement rates and extent, mobilised volume and future slope failures.

- Synthetic Aperture Radar interferometry (InSAR) technology is based on data acquired by SAR systems. Synthetic Aperture Radar (SAR) is an active microwave device capable of recording the electromagnetic echo backscattered from the Earth surface and of arranging it in a 2D image map.

This type of sensors can be mounted on spaceborne platforms, with up to cm resolution (e.g. RADARSAT, LANDSAT TM, QUICKBIRD), or on terrestrial devices with resolution up to mm.

InSAR principles rely on the fact that SAR images contain information about the sensor-target distance. A pixel by pixel comparison performed on various SAT products with different collection dates can identify areas where the ground has deformed (Colesanti & Wasowski, 2006) and yields satisfactory results when monitoring slopes and objects which move with at low speed.. However, changes in the vegetation cover and different atmospheric conditions at the collection times can hamper the quality of the result (Niebergall et al., 2007).

- A LIDAR (Light Detection And Ranging) system uses a powerful laser sensor, a GPS receiver, and an INS unit to record the elevation of the terrain being scanned. The laser sensor is placed in the bottom of a flying device. Once airborne, the ranges to points on the ground are determined by means of infrared laser light emitted by the sensor as rapid pulses. The ranges are processed together with the GPS/INS information to determine the elevation of the terrain (ERDAS, 2010). Laser scanning is currently applied in many fields as a contactless method for determining spatial coordinates, including monitoring of geomorphological. During the laser scanning process, a large number of points are measured within a predefined grid covering the area of interest. It is, therefore, a particularly suitable method for generating digital terrain models (Burda, Hartvich, Valenta, Smítka, & Rybář, 2013)

- Historical aerial photographs are a valuable resource to trace back changes in landscapes that have occurred years before an area becomes subject to study. As early as World War I, the first aerial survey camera was developed. Initially applied as a reconnaissance tool, its use extended to other fields, as forestry, agriculture and archaeology. After World War II, advances made by warring countries, especially aerial triangulation, allowed the development of basic mapping techniques. Photogrammetry, described as the technology to derived geometric information of objects with the help of image measurements, was first based on stereoscopic pairs (two aerial pictures that partially overlap), which are visually inspected under a set of lenses and mirrors, enhancing the illusion of depth and offering information about the relief of the area under study. The introduction of computer into photogrammetry in the 1950s meant the automation of triangulation and a noticeable gain in accuracy and reliability, but it was in the 1980s when digital photogrammetry became a very powerful tool for orthorectification of images and map production (Konecny, 2003).

Data obtain via remote sensing tools is usually processed and analysed in the context of Geographic Information Systems (GIS). GIS is defined by Star & Estes (1990) as "an information system that is designed to work with data referenced by spatial or geographic coordinates. In other words, a GIS is both a database system with specific capabilities for spatially-referenced data, as well as a set of operations for working with data. In a sense, a GIS may be thought of as a higher-order map." In the frame of geomorphological studies, GIS is a tool for the generation of elevation models of the area of interest (DEM). Digital Surface Models (DSM) represent the earth surface including objects present on it, such as buildings and vegetation. Digital Terrain Models (DTM) approximate the topography of the surface, removing the effect of these objects.

3. Research area condition

The extreme rainfall events on the first days in January 1994 (98.5 mm in 6 days) after a very wet winter (see figure 3.2) triggered a mass movement near the Charonnier river, located near the towns of Veynes and Gap in the French department of Hautes-Alpes (Figure 3.1). The Charonnier river is a tributary of Le Drouzet river, which drains in Le Petit Büech, and via the Büech reaches the Durance river, which drains in the Rhone to finally drain in the Mediterranean sea by the town of Port-Saint-Louis-du-Rhône. The access to the landslide can be made via the road connecting Veynes with Esparron.

3.1 Geology and geomorphology

The study area is located in the Western Alps, the most occidental division of the Alps, limiting to the Mediterranean Sea in the South and reaching the Lake Geneva to the North, and stretching over 150km in the east-west direction. The studied landslide is more specifically situated in the catchment of the Büech River, in the subalpine zone (Figure 3.1)

The geology of the region is the product of a combination of Pyreneo (70 Ma to 34 Ma) and Alpine (30 to 2 Ma) orogenic activity, that folded materials deposited during the Mesozoic Era (251-66 Ma). The relief was later shaped by morphodynamic processes during the Würm glaciation, when morainic material was deposited in the main valley bottoms.

The Charonnier landslide developed on Upper Jurassic material. Thick layers of dark marl (locally named “Terres Noires”) deposited during the Oxfordian in an extensive basin submerged by the Mediterranean Sea delimited in the West by the Rhône valley, in the North by the latitude of Grenoble, in the East by the Italian border and in the South by the Provence Prealps. During the Kimmeridgian and Tithonian massive limestone layers (“Calcaire Tithonique”) were deposited (Maquaire et al., 2003).

The lithology of the region characterized by alternating marl and limestone deposits from the Jurassic and Cretaceous periods. “Terres Noires” can be split into three units: the oldest material, from upper Bajocian to lower Bathonian consists of black marls, cut into fine platelets; the intermediate unit (upper Bathonian and lower Callovian), which is harder, consists of clayey and dolomitic limestone with a brownish platina; and the upper layer (Oxfordian) also comprises black marls cut into platelets and incorporates carbonated nodules. Physical and mineralogical properties of the formation conclude that the lower and upper units of the series are very similar, so “Terres Noires” can be considered as a homogenous lithological mass (Antoine et al., 1995a).

Material from the Upper Oxfordian, known as “Argovien”, marks the transition to the “Calcaire Tithonique”. The Argovien unit consists of a series of layers, being the lower ones mostly marls and more limestone being present in the younger layers.

Climate change during the last part of the Quaternary drove the last morphological processes that shaped the landscape in the Alps, together with human activity. During the first half of the Holocene, after the last glacial period, climate conditions prompted the start of an aggregation period, where sediments filled the bottom of many secondary basins, while a near complete forest covered the Büech basin. During the second half of the Holocene human settlements began, coincident with a more erosive period and shorter climatic oscillations. A rise in human activity in the Neolithic resulted in the first signs of deforestation and overgrazing. In

recent times (last 10 centuries), small-scale climatic oscillations, together with an aggressive human activity (Kappes et al., 2011) that caused an important deforestation, have hastened morphological changes, with evidence in river systems where river beds has widened, gravel bars have formed and braided patterns are now visible (Descroix & Gautier, 2002).

In the last decades, human pressure has decreased and forest area has expanded. However, gullies and badlands are still visible in eroded areas, showing morphological processes and surface changes.

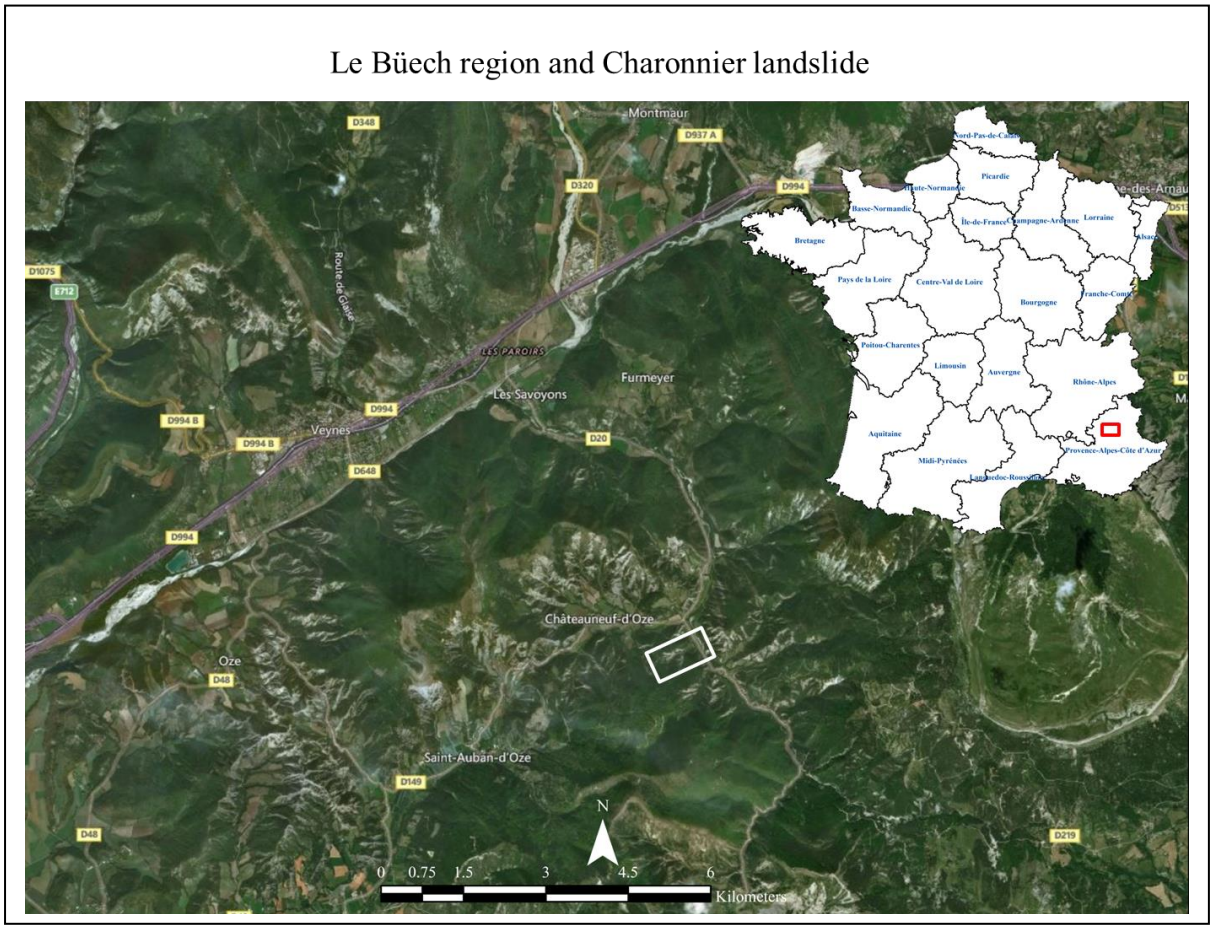

Figure 3.1. Map of the Büech region. Charonnier landslide location is encase in the white rectangle and approximately 20km south-west of the city of Gap.

3.2 Meteorology

The Hautes-Alpes province is located within an Alpine climatic zone influenced by Mediterranean conditions, characterized by great seasonal variability. Summers are hot and dry, with rainfall accumulated in high-intensity events, and an average temperature of 24°C. Autumn months are the most humid ones (September, October, and November) and precipitation in winter is often in the form of snow, which results in extra water in the mountain systems during the melting season in Spring. Average winter temperature is 7°C, but the presence of abundant thaw-freeze cycles increases the erosion capacity of runoffs (Descroix & Mathys, 2003; Maquaire et al., 2003).

3.3 The 1994 event

Field observation of the Charonnier landslide suggests that the mass wasting process that took place on the 4th of January of 1994 circumscribes to the interface of "Terres Noires" and marls with higher limestone content ("Argovien"). Other mass wasting processes took place in the Buëch catchment area during the same season triggered by intense rainstorms on October 1993 and January 1994 (Antoine et al., 1995b; Maquaire et al., 2003; Pech & Sevestre, 1994), affecting other outcrops of "Terres Noires", where already saturated soils receive a water addition. The analysis of the precipitation report from the meteorological station in Tallard, 8 km east of the Charonnier landslide determines that the antecedent rainfall recorded between the 2nd of January and the 8th of January 1994 (98.5 mm) corresponds to a return period of 2 years, and 138.4 mm antecedent precipitation was recorded between October 5th and 10th with a return period of 8.25 years, only surpassed by multiple day rainfall events in 1997, 1999 and 2002. For the period September 1993- January 1994 a total of 626 mm precipitation was recorded. Even for the wet autumn/winter months, this is a significant amount of precipitation, despite November being the second driest recorded (De Vries, 2017) (See figure 3.2).

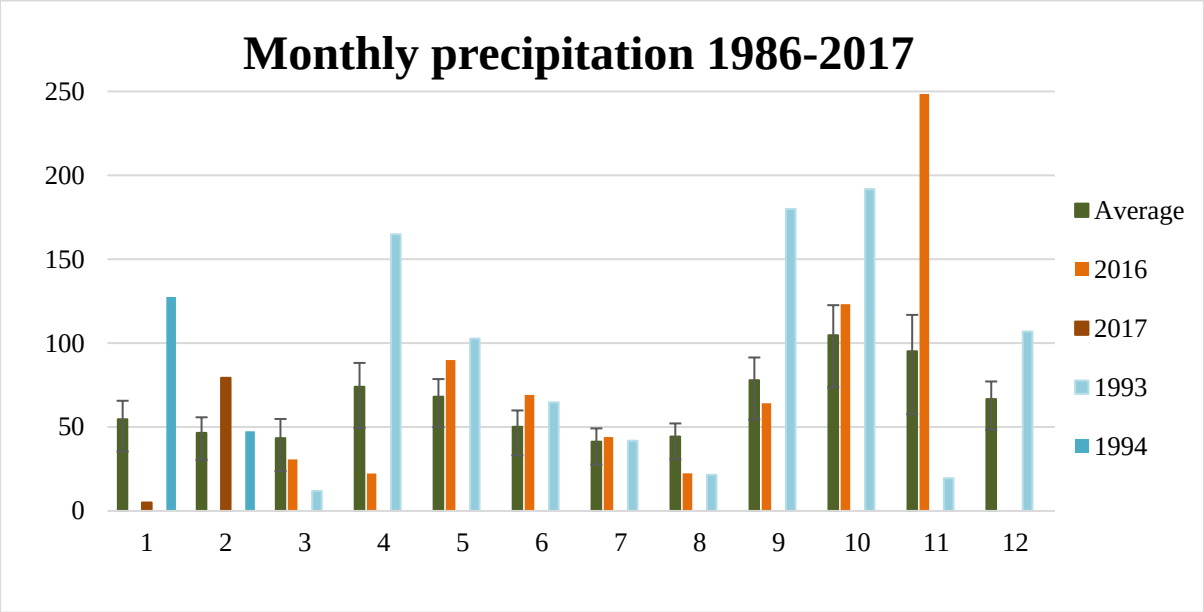

Figure 3.3 Average monthly precipitation recorded in the meteorological station in Tallard between 1986 and 2015 (green bars; error bars represent the standard deviation). Precipitation recorded in the seasons 1993-1994 and 2016-2017 are displayed in blue and reddish bars, respectively.

4. Methods & Data

In the study of the Charonnier landslide, efforts are devoted to studying the stability of the landslide and its possible movement or deformation over the last year, as well as in the long-term, since the 1994 event.

Remote sensing has been proven as a suitable tool for different objectives: landslide risk zonation, reconstruction of morphological changes over time and ground deformation detection, among others. In the present study, a multi-temporal set of UAV based images and historical aerial pictures is used for the construction of point clouds, orthoDEMs and orthomosaics that capture the topography of the Charonnier landslide location and its surroundings in different dates throughout the last 25 years.

In situ observations and geotechnical procedures allow the determination of other parameters and soil properties affecting landslide stability. Controlling mechanism and soil parameters as infiltration capacity or volumetric water content are determined upon field measurements.

The study of the dynamics of the Charonnier landslide can be divided into 2 stages: first, field work carried out in France during June of 2017; and second, data processing and analysis performed in Utrecht, the Netherlands, in subsequent months.

De Vries (2017) and Van Haaster (2017) collected in June 2016 very high-resolution UAV based images and produced orthoDEMs and orthomosaics. Soil samples were also gathered and analysed, and soil parameters inferred. Their results are also incorporated to the present study since they offer information about the state of the landslide in June 2016.

4.1 Remote sensing and photogrammetry

The application of remote sensing techniques appears as an efficient approach to obtain terrain elevation data and detect morphological changes that could be linked to the reactivation of the landslide, such as displacement of boulders or other elements within the body of the landslide, appearance of cracks in the toe, creep in the flanks, modification of the crown trace or subsidence in the head area.

By DEM differentiation, elevation change on the landslide surface can be detected and mobilized volume calculated (Van Haaster, 2017). However, this approach is highly dependent on the resolution of the imagery and the produced DEM compare to the magnitude of the height variation and can be not useful to detect changes in very steep locations with near vertical surfaces. Efforts to study ground deformation have led to the development of some algorithms: CossiCor algorithm (Lucieer et al., 2014; Turner et al., 2015), computes horizontal displacement on the landslide by means of the tracking of homologous parts of the surface, and it can yield good results when internal deformation of the moving mass does not prevail (rotational slides and creep). Another new procedure to detect and monitor ground deformation, often used with LIDAR-based dense point clouds (DPC), is cloud to cloud comparison (Busker, 2017; Cook & L., 2017). M3C2 algorithm (Lague et al., 2013) uses two dense point clouds acquired on different dates as input and measures the distance between them.

The present research employs two types of photographic resources to generate elevation information and detect topographic changes in the Charonnier landslide in both short-term and

long-term time scales, from 1993 to 2017: historical aerial pictures and UAV-based imagery from 2016 and 2017 campaigns. Two different methods for topographic change detection are evaluated: cloud to cloud comparison with the M3C2 algorithm and DEM differentiation.

4.1.1 Elevation information from UAV images

During the field work stage in June 2017, a flight campaign is scheduled in order to take pictures that cover the Charonnier landslide area, together with the placement of markers on the terrain, that are used as ground control points (GPC). This data is used

4.1.1.1 UAV image acquisition

Low altitude aerial photos are collected with a Canon compact digital camera (Powershot D10, focal length 6.2 mm and 12 MP resolution) installed in a polystyrene fixed wing flying platform with a span of 2 metres. The sensor captures pictures in JPEG format with a lossy compression, reducing the size of files. This material is the same used by De Vries (2017) and Van Haasten (2017), and flying strategy is also based on their campaign to guarantee comparison of the 2016 and 2017 datasets.

Figure 4.1 Employed fixed wing UAV in the hands of the technician who operated it.

During the image acquisition phase, in order to achieve a maximum image quality, flight stability and flight height are important. Other factors can also reduce the quality of the photographs, as rain or big shades on the terrain (Lillesand et al., 2015). Ideally, image acquisition should be performed in one day, so light conditions are constant and around central hours of the day in order to avoid big shades.

However, rain and excessive wind speed impeded the complete coverage of the landslide area within one day. 8 flights were completed between June 4th and 8th 2017, with an average flight time of 12 min and an average flight height of 115m, capturing in total 1091 pictures, from which 850 are used in the photogrammetry process. Photos are selected on the basis of their quality and coverage of the area under study: blurred, too bright images or the ones covering the sky or areas further away from the landslide are excluded from the photogrammetry process.

4.1.1.2 Markers for SfM

Given that a non-metric Canon compact camera was used, with unknown internal orientation, a reference system had to be created to be able to determine 3D locations within the photos. As opposed to the traditional photogrammetry this doesn't have to be done with camera settings and triangulation. Instead, control points can be identified within the image with geographical coordinates (x, y and z), allowing the camera position to be determined for each photo (Westoby et al., 2012). For this reason, a total of 69 clearly distinguishable markers are placed and measured with a Trimble differential GPS unit. These measured locations are Ground Control Points (GCP) in the following image processing stage in Agisoft Photoscan. With the use

of a differential Global Positioning System (DGPS) the GPS signals are accurately surveyed up to centimetre accuracy (Smith et al., 2016). The differential GPS uses a modem to correct received satellite locations with satellite locations to a stationary location with known coordinates. Because each of the signals received contains a certain error a stationary measurement device can correct the received signals in the field. The coordinates are referenced into the UTM 31N WGS84 reference grid.

Additionally, locations of 11 distinguishable features on the landscape (crossroads, bridges) are measured with the same instruments. These positions, spread over an area of 20 km2 are control points for the photogrammetry process executed on ERDAS IMAGINE (ERDAS, 2010) , as it is detailed in the 4.1.5.

4.1.1.3 SfM processing

Agisoft PhotoScan (Agisoft, 2017)is the software chosen to perform the photogrammetric processing of the collected UAV-based images due to its capability to generate 3D spatial data to be used in GIS applications and its user-friendly interface (Immerzeel et al., 2014; Van Haaster, 2017) . The image processing workflow (Figure 4.2) starts with the link and overlap of the photographs based on the scale invariant feature transform (SIFT), an advanced image feature recognition technique that automatically detects, describes and matches characteristic objects between photographs (Lucieer et al., 2014; Turner et al., 2015; Westoby et al., 2012). Prior to the image alignment, areas covered by vegetation are masked (polygons are drawn for every image, covering the pixels with dense vegetation), so they are excluded from the feature recognition, which only detects coincident key features from the bare soil. Then, the matched features are required for a bundle-block adjustment, which identifies the 3D position and orientation of the cameras and the location in the X, Y and Z coordinates of each image feature, creating a sparse 3D point cloud. A subsequent densification technique is then applied to derive very dense 3D models (dense point cloud, DPC). The use of ground control points (GCPs) is required to georefer in a real-world coordinate system the 3D model. First output of the image processing is dense point cloud, which includes vegetation cover and ground surface. From this DPC, Agisoft Photoscan generates a digital surface model (DSM), with a spatial resolution fixed by the user. In order to obtain a digital terrain model (DTM), where vegetation cover is excluded, aiming to represent ground elevation, points corresponding to vegetated areas in the DPC are manually removed. The software offers a tool for point selection by colour, that has been tested, but hasn't yield accurate results. From the modify DPC, an orthoDTM is obtained. Finally, an orthomosaic is derived from the blended images, using the DSM as elevation reference.

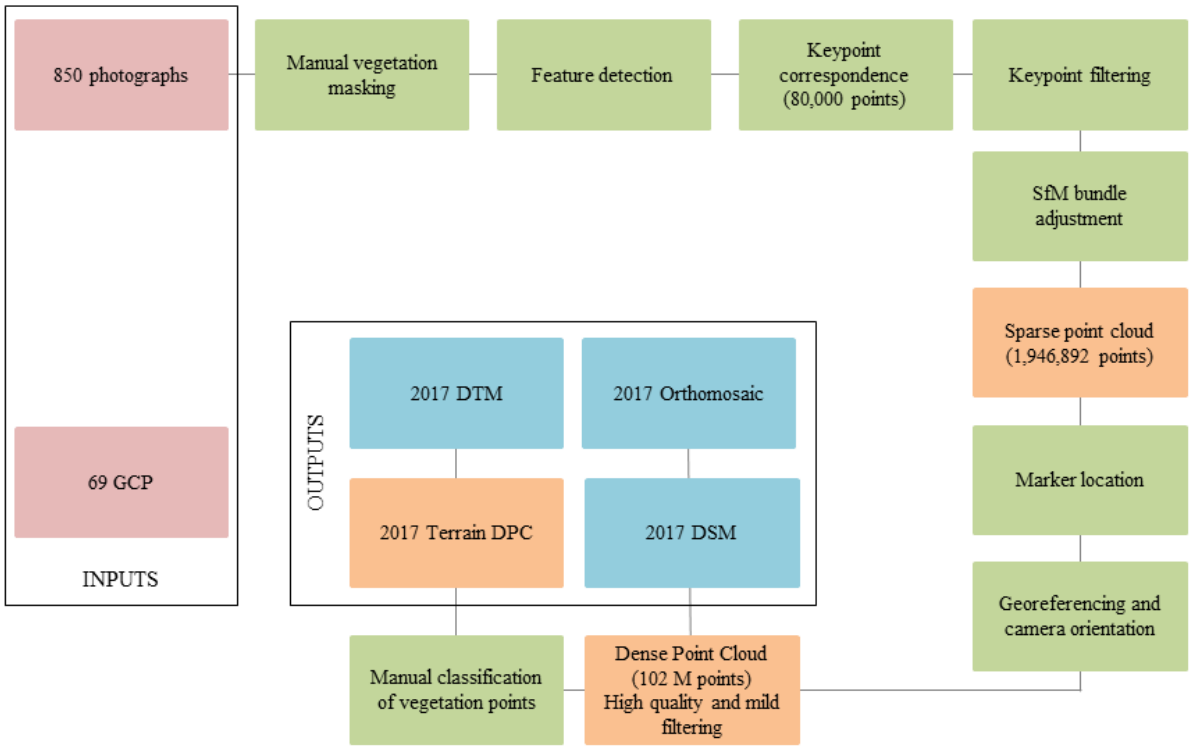

Figure 4.2 Flowchart of the photogrammetry project carried out with Agisoft Photoscan software from 2017 UAV based images of the Charonnier landslide.

4.1.2 Elevation models from historical aerial photographs

The availability of historical aerial photographs that cover the area of the Charonnier landslide allows the reconstruction of the site pre-landslide topography and DEMs with stereophotogrammetry techniques (Dewitte et al., 2008). The Institut national de l'information géographique et forestière (IGN) offers at its website access to raw aerial pictures including the Charonnier landslide and its surroundings in years 1948, 1956, 1971, 1978, 1981, 1982, 1985, 1993, 1995, 1997, 1998, 1999 and 2003, with a maximum resolution of 900dpi.

The resolution of the imagery used in photogrammetry plays an important role in the accuracy of the triangulation and orthorectification stages in the process. Therefore, the scanning resolution is an important factor to consider in order to optimize the accuracy of the final result (ERDAS, 2010).

High quality printed copies of the stereoscopic photos corresponding to the 1999 flight are available at Utrecht University Library Special Collections, and permit a high-resolution scanning that, together with the available camera report, may yield high accuracy outcomes of the photogrammetry process, as explained in the next sections .

4.1.2.1 Photogrammetry in LPS Project Manager

A new project is started with the help of LPS (Leica Photogrammetry Suite) Project Manager, software developed by ERDAS to rectify aerial pictures, in which input data are the scanned 1999 stereopair with a resolution of 2400dpi, location of 11 ground control points collected in June 2017, and flight information from the camera report (Figure 4.3).

LPS Project Manager applies the collinearity equation in the modelling process, which rectifies the images by combining camera orientation, relief movement and the Earth's curvature. The orthorectification process in LPS Project Manager produces planimetrically true orthoimages with the geometric characteristics of a map and photographic image quality (ERDAS, 2010).

Workflow in LPS Project Manager system starts with the creation of a block file, in which photographs covering the area under study are included and Reference Coordinate System is specified. Second, interior orientation parameters described in the available camera report are inserted. The interior orientation defines the internal geometry of the camera as it was at the time of image capture by means of 4 variables: focal length, lens distortion, fiducial marks and principal point. The transformation of the image pixel coordinate system to the image space coordinate system requires the use of the variables describing the interior orientation (ERDAS, 2010). In this case, focal length of the camera is 152.754mm, lens distortion is negligible, and coordinates of 8 fiducial marks are given as well as principal point value (table 4.1).

Table 4.1Fiducial marks and Principal Point coordinates included in the interior orientation. Source: Camera report 144112, IGN

	X (mm)	Y (mm)
Fiducial number		
1	113,005	0,013
2	-112,990	0,002
3	0,004	113,016
4	-0,007	-112,981
5	113,000	113,013
6	-113,001	-112,990
7	-113,993	113,004
8	113,001	-112,987
Principal Point	0,005	0,001

The exterior orientation defines the position and angular orientation of the camera that took the image by means of three angular or rotational elements: omega (ω) is a rotation about the photographic x-axis; phi (ϕ) is a rotation about the photographic y-axis; and kappa (κ) is a rotation about the photographic z-axis. This way the ground space coordinate system (X, Y, and Z) can be related to the image space coordinate system (x, y, and z). When these values are missing, they are derived in the triangulation stage. LPS Project Manager uses bundle block adjustment techniques for formulating the relationship between image space and ground space based upon the collinearity condition, which defines that the exposure station, the point on the ground, and the corresponding point location in the image must all align (ERDAS, 2010).

4.1.2.2 GCPs for orthorectification

GCPs are identifiable features located on the Earth's surface with known X, Y, and Z ground coordinates, and which allow the formulation of an accurate relationship between the ground, the camera and the images used in the project. For the survey of Charonnier landslide, coordinates of 11 identifiable locations where recorded during the field campaign in June 2017 over the area (approximately 100km^2) covered by the selected aerial photographs (Appendix II). These positions correspond to features at roads and trails, as bridges and road intersections, that are supposed to be invariant since, at least, 1999. LPS Project Manager can automatically identify and collect more points present in both photographs and measure their image position. Tie points are points visually recognizable in two or more images that overlap and whose ground coordinates are unknown. Once that GCPs ground and image coordinates, tie points image coordinates and internal orientation are specified, aerial triangulation is performed, establishing the mathematical relationship between the photographs included in the block file, calculating the exterior orientation and tie points ground coordinates.

4.1.2.3 Terrain extraction from stereoscopic pairs.

LPS Automatic Terrain Extraction (LPS ATE) is functionality within the LPS project Manager System that allows the extraction of elevation information after the triangulation process. Using a robust algorithm, LPS ATE compares two images and looks for the image positions of conjugate features appearing in the overlap portions of the images. Ground points appearing within the overlap portion of the images are identified and their coordinates computed through a space forward intersection technique (ERDAS, 2008), turning into a point cloud (DPC). The DPC is already a geographically correct product that can be extracted as LASER format (.LAS) and be analysed by means of other GIS tools, as it is explained in the section 4.1.7.

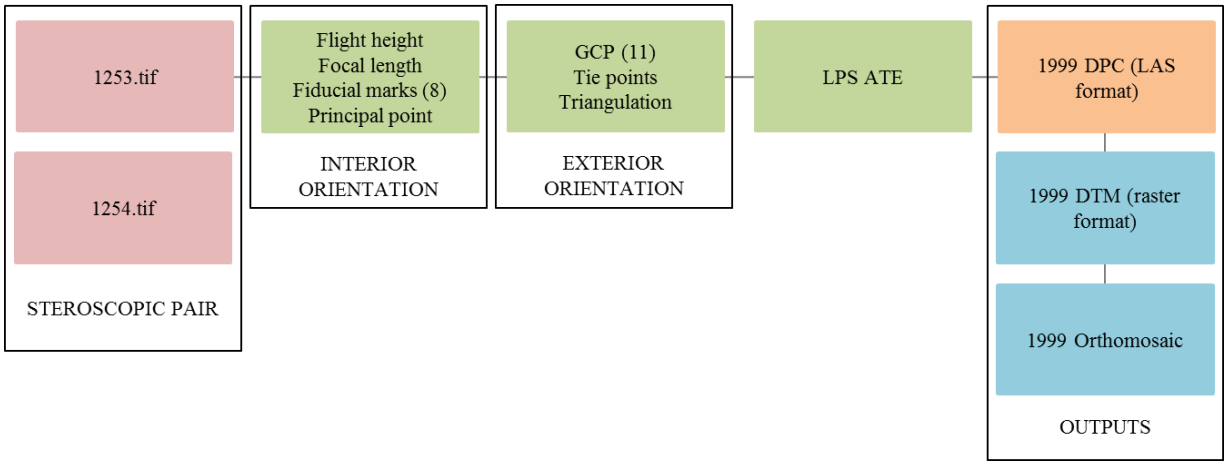

Figure 4.3 Flowchart of the photogrammetry project carried out with ERDAS LPS Project Manager from 2 stereoscopic pictures that cover the Charonnier landslide and its surroundings in 1999.

The raster DEM output option in LPS ATE creates a continuous DTM representation of the surface of the Earth by means of the interpolation of DPC elevation values to create a raster grid DEM. Interpolation method and output cell size are determined by the user. The generated DTM is finally used by LPS Project Manager as elevation information source for the ortho resampling of the aerial photographs, generating an orthomosaic of the area where they overlap.

4.1.3 Calculation of the displaced soil volume

An estimate of the volume of material displaced by the landslide in 1994 is compute based on the outputs in raster format of the photogrammetry processes.

Orthomosaics and DTMs dated 1993 and 1999 represent the state of the Charonnier landslide site before and after the 1994 event. The differential DTM displays in a cell-by-cell basis the topography decline in units of length of the source area caused by the mass movement in 1994. A polygon that limits the source area is drawn, and the volume comprised between the 1993 and 1999 surfaces is computed as the summation of all the cell values times the cell size.

4.1.4 Dense point clouds and digital elevation models

Photogrammetry projects carried out in Agisoft Photoscan and LPS Project Manager environments generate elevation models of the Charonnier landslide in the form of DTM and orthomosaic in raster format, and DPC (.LAS) dated 1993, 1999, 2016 and 2017. With the analysis of these products, topographic changes linked to the dynamics of the landslide in the short and long term can be detected. To do so, two strategies are implemented: (I) DTM subtraction; (II) distance calculation between DPC.

I) Elevation models in raster format (DTM) and orthomosaics are visualised by means of ArcMap software. This GIS tool allows the statistical and spatial analysis of this kind of datasets, and the generation of new files as a product of a combination of pre-existing ones. In the current study, 3 final products are generated through the subtraction of the value of a DTM from the value of another one dated earlier on a cell-by-cell basis: 1993-1999, 1999-2017 and 2016-2017. 1993 DTM and 2016 DTM are available from previous research (De Vries, 2017; Van Haaster, 2017). For 1993-1999 subtraction, cell size of the output raster is set the same as the inputs; the same approach is followed in the 2016-2017 case. However, it needs to be noted that cell size of 1999 DTM is different from 2017 DTM, and output product resolution is determined by the coarsest of the input datasets (1999 DTM).

II) Distance calculation between two point clouds is especially useful when homologous parts cannot be defined, typical of natural surfaces altered by erosion or sedimentation between surveys (Lague et al., 2013). The comparison between DPC follows the same time structure, and it is performed via CloudCompare software and the Multiscale Model to Model Cloud Comparison (M3C2) algorithm developed by Lague et al. (2013). The M3C2 method consist on two stages: first, "the surface normal estimation and 3D orientation adapting the scale to the local surface roughness; and second, the computation of the mean surface change along the normal direction together with the calculation of a local confidence interval "(Lague et al., 2013)(Figure 4.4). Compared to raster-based comparison methods, M3C2 algorithm has been used due to its ability to handle differences in the X, Y and Z axis in complex topographies (vertical and flat surfaces on the same scene) and to overcome the uncertainty related to point cloud roughness by calculating averages in a local scale (Busker, 2017; Cook, 2017).

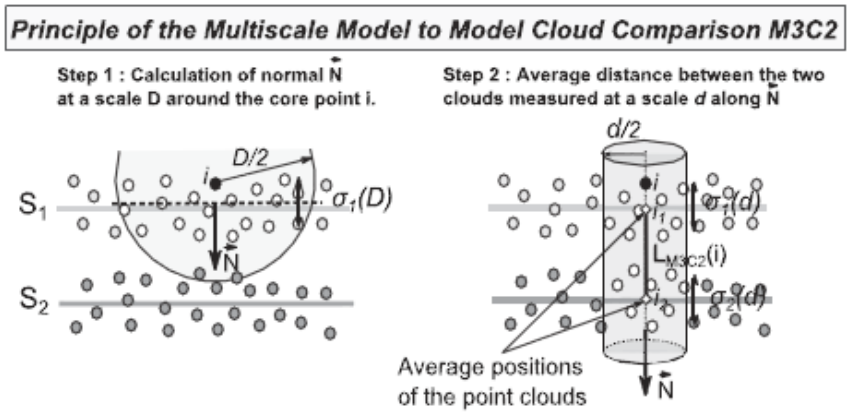

Figure 4.4 Description of the M3C2 algorithm and calculation of normal orientation (N) from Lague et al. (2013): "Step 1: The normal is estimated from cloud 1. Step 2: 2 sub-clouds are defined by the intersection of the reference and compared clouds with a cylinder of diameter d and axis (i, N). Each sub-cloud is projected on the cylinder axis which gives a distribution of distances along the normal direction. These are used to define the mean (or median) position of each cloud i_1 and i_2"

Drawback of this method is the difficulty to choose the value for the normal scale (D) parameter; for rough surfaces, the orientation of the normal can greatly vary if the scale at which is measured is too small in relation to the surface roughness. This situation will lead to an overestimation of the distance between the two point clouds. On the other hand, if normal scale parameter is too high, topographic characteristics of the surface can be ignored, and calculation of the distance between clouds is underestimated. In this case study, D is manually tweaked until distance between clouds starts showing values different from 0. A value of 1m for D is too high, and no distance is detected, since in this case study, topography changes from 2016 to 2017 due to erosion are in the order of cm, and they would be neglected. Use of M3C2 algorithm is also limited by its requirement of high computer performance. For point clouds with considerable point density, it may be advised that cloud distance computation is only performed in selected and delimited areas.

4.1.5 Accuracy assessment

The accuracy of the products of the different photogrammetry processes is assessed with different methods depending on the capabilities of the applied software and on the output format.

4.1.5.1 Raster products form aerial photographs 1999

The orthomosaic and orthoDTM obtained with the help of LPS Manager displaying the state of the landslide in 1999 have a coarse resolution due to the limited resolution of the input aerial photographs. Then, after the triangulation process in LPS manager, the software computes the accuracy of the orthoDTM as the Root Mean Square Error (RMSE). It is not effective to make a manual estimation of the quality of the output by means of control points (as it is explained in the next section) because the pixel size of the produced DTM is bigger than the error, so is not detectable following this approach.

When estimating the volume of the displaced material, the uncertainty associated to the DTM is incorporated in the volume uncertainty by calculating the volume corresponding to an area analogous to the source area with a height component (or cell value) equal to the RMSE of the less accurate DTM (1993).

4.1.5.2 Raster products from UAV images 2017

In order to assess the accuracy of the DTM created with the help of Agisoft Photoscan, 13 independent GCP are used, whose location is shown in Figure 5.5. The error in the X, Y and Z direction is measured between the GCP location in the orthomosaic and the coordinates of the markers measured in the field. The direction of the error is shown as the angle between the GCP location in the orthomosaic and the measured coordinates in the XY directions. Overall accuracy is the average of the error in each of the independent GCP.

4.1.5.3 Dense Point Clouds

The accuracy of the Dense Point Cloud constructed from UAV images and from aerial pictures is assessed with identical methodology after the distance between clouds has been computed with the M3C2 algorithm. The vertical resolution of 1993 and 1999 DPCs is determined jointly, as the offset between both point clouds in a reference area at the road, which is assumed

to have constant height. The distance between point clouds there is taken as the error in the vertical axis for the M3C2 distance calculation output.

In the case of the calculation of the distance between 2016 and 2017 DPCs, the vertical accuracy is determined in the same way, using the same area at the road as the invariable surface, but using 2016 DPC and 2017DPC as input.

4.2 Soil characterization

Characteristics of the material that defines the Charonnier landslide are retrieved by in-situ measurements and laboratory procedures. Measurements and sampling location should be representative of the different parts of the mass movement, so the definition of parameters can be done attending their spatial variability (Caris & Asch, 1991; Van Asch et al., 2009). Sampling strategy and analysis techniques are established upon the procedures carried out in June 2016 by the previous research group that studied the Charonnier landslide (De Vries, 2017; Van Haaster, 2017). Emulating their approach and using the same instruments aim to reduce experimental error, obtain accurate measurements and allows comparison and merging of the datasets. The landslide surface is divided into two distinct areas: an area in which parent material is, as of now, undisturbed and keeps the physical and mechanic soil characteristics at the time of the first landslide event in 1994, and an area where slumped material has been deposited after the mass movement event and after have been subjected to physical and chemical processes that may have modify their characteristics.

In June 2017, 29 core samples were collected to determine dry bulk density (DBD), volumetric water content (VWC) and the soil retention curve (SWRC). Five inverse auger tests were carried out in order to obtain saturated conductivity (K) values. Sampled material from the 2016 campaign, by De Vries (2017), is also available in Appendix IV.

Field and laboratory methods are explained in the next sections.

4.2.1 Saturated hydraulic conductivity

This parameter represents the maximum rate of flow in saturated conditions. Hydraulic conductivity values are determined in-situ by means of inverse auger hole tests: a vertical borehole, deep enough to reach the layer of soil subject to characterization , is drilled with an auger and filled with water several times. Water infiltrates to the soil rapidly at the beginning, draining the borehole, till water infiltration becomes slower and constant, this indicates that the surrounding soil is now saturated. The hole is completely filled with water again, and the test starts. The constant drop of the water level is measured with a float and a timer and it is used to determine the saturated hydraulic conductivity according to:

$$K = 1.15\ r\ \frac{\log(h0+\frac{1}{2}r)-\log(ht+\frac{1}{2}r)}{t-t0} \qquad (8)$$

With K (m) being the hydraulic conductivity (m/day), r the radius (m), t is the time (s) since the start of measuring, ht the height (m) of the water column and h0 the value at start of measurement.

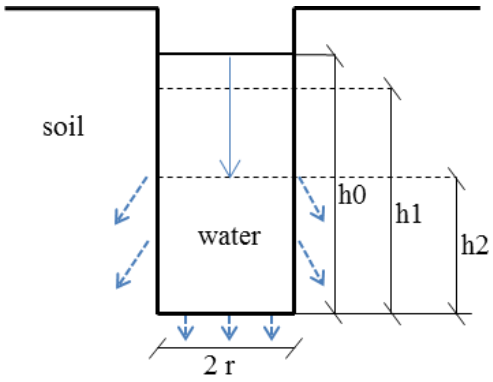

Figure 4.6 Invers auger hole test. h0 represents the height of the water column at t=0. Water infiltrates to the surrounding soil and the height of the column is measured again at t=1,2…n (h1, h2… hn).

Macro-pores in the soil can hamper the accurate determination of the conductivity parameter, leading to an overestimation (Youngs, 2000), so only tests with a constant drawdown of the water level are considered in the estimation of the saturated conductivity. 5 successful tests are performed, lasting an average of 60 min each one (table 4.2). Water drawdown is recorded every 10 seconds during the first minutes, decreasing the measuring frequency when the change in water level becomes slower and ultimately constant.

Table 4.2 Record of samples from 2017 campaign.

	Cores	Undisturbed samples	Inverse auger test
n	25	18	5
Depth range [cm]	0-77	0-50	35-77

4.2.2 Dry bulk density

This property represents the density of the soil excluding water, and relates to the amount of infiltration and the stability of the slope. Volume of the soil particles and pore volume can be inferred from dry bulk density and gives information about the permeability of soils to air and water (Cammeraat et al., 2001).

Samples of 100cm3 are collected in steel Kopecky rings of 5cm high and 5cm of diameter from representative locations of the landslide and sealed to preserved moisture conditions and structure of the material. A total number of 29 samples are gathered from the two distinct areas (shown in figure 4.7), weighed (including the metal ring and a tin basket containing the soil material), and oven dried at 105°C for 24h hours.

Afterwards, samples (including the containers) are weighted, as well as the containers themselves. The weight of the dry material (Ms) related to the volume (V) indicates the DBD (Campbell & Henshall, 2000).

$$DBD = \frac{M_S}{V} \quad (9)$$

The amount of water at field capacity in the sample can be calculated by the loss of weight by drying. This can be either expressed as volumetric water content per known volume or gravimetric water content per mass of dry soil. The subtraction of the weight of the dry samples and the ring and basket from the initial weight gives the gravimetric water content of the soil.

Related to the dry bulk density (soil dry weight/soil volume), the volumetric water content is calculated:

$$\theta = \frac{w\ DBD}{\rho w}, \qquad (10)$$

where θ is the volumetric water content, w the water content and ρ_w is the density of water.

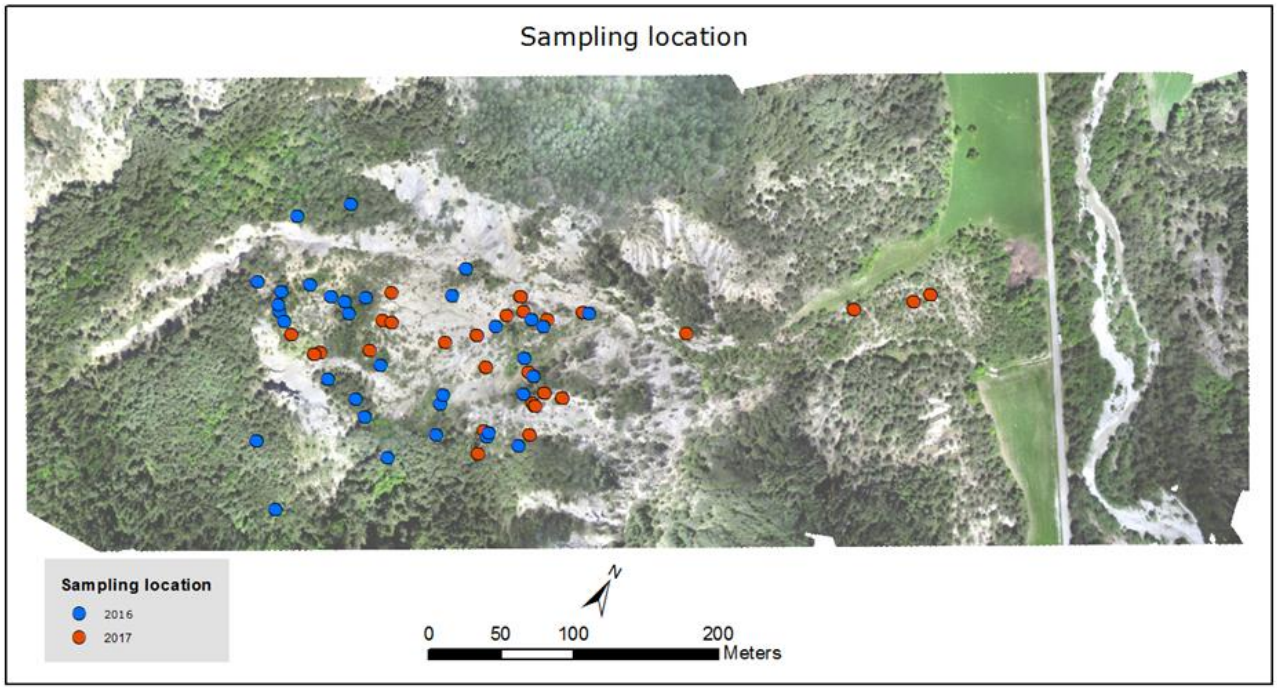

Figure 4.7 Location of the retrieved soil samples over the Charonnier landslide area for the laboratory tests.

4.2.3 Statistical significance of soil characterization results: t-test

Although sampling strategy and sample size are comparable between the 2016 and 2017, collection locations and researchers carrying out the sampling process are not the same.

Given these differences, plus the fact that sample size for both years is limited, values of the soil parameters inferred from the explained soil tests for both years must be compared in order to obtain possible spatial and temporal patterns and their statistical significance. In order to stablish the statistical significance of the difference in the parameters, a t-test for two independent samples is performed for each parameter, comparing the results for both years, for parent material from the source area and slumped material from the accumulation area separately. Sample average value, sample standard deviation and sample size are known. Null hypothesis (H0) is stated as:

$$H_0: \mu_{2016} = \mu_{2017}, \qquad (11)$$

while the alternative hypothesis (H1) is:

$$H_1: \mu_{2016} \neq \mu_{2017} \qquad (12)$$

A level of significance $\alpha = 0.0.5$ is chosen, assuming both normal populations have the same standard deviation. The test statistic used to test the null hypothesis, with degrees of freedom $\nu = n_{2016} + n_{2017} - 2$, is:

$$t_0 = \frac{\bar{X}_{2016} - \bar{X}_{2017}}{S_p \sqrt{\frac{1}{n_{2016}} + \frac{1}{n_{2017}}}} \quad (13)$$

where $\bar{X}$ is the sample average, n is the sample size and S_p is the pooled estimation of the variances σ^2, and it is defined by

$$S_p^2 = \frac{(n_{2016}-1)S_{2016}^2 + (n_{2017}-1)S_{2017}^2}{n_{2016}+n_{2017}-2} \quad (14)$$

where S^2 is the sample variance.

If $t_0 > t_{0.025,\nu}$ or $t_0 < -t_{0.025,\nu}$, the hypothesis H_0: $\mu_{2016} = \mu_{2017}$ is rejected.

The test is used for comparison of the mean values of the described parameters between both years, first differentiating parent and slumped material.

Then, 2016 and 2017 samples are pooled to infer the statistical significance of the difference of soil properties between the accumulated and the source area (Table 5.2) applying, as above, a t-test.

5. Results

The aim of this study is to identify the main dynamic processes acting in the Charonnier landslide since 1993 (before the mass movement in 1994), to detect possible dynamics between 2016 and 2017 and to compare and analyse two different methodologies for topographic changes measurement.

Following this objectives, dense point clouds (DPC), DEMs in raster format and orthomosaics constructed through the processing of UAV-based images and historical aerial photographs are analysed on the basis of their capability to detect the morphological differences on the landslide throughout 24 years (1993- 2017). Soil properties retrieved from sample processing are compared between years and areas to stablish possible spatial or temporal trends related with the geomorphological processes.

5.1 Landslide dynamics and remote sensing

The dynamics of Charonnier landslide are assessed for three different time periods throughout the landslide history: before and after the initiation in 1994, the dynamics between June 2016 and June 2017, and processes between 1999 and 2017.

5.1.1 Detection of the volume displaced by the landslide in 1994 from 1993 and 1999 aerial photographs.

Two different methodologies are applied for the detection Digital Elevation Model subtraction and Cloud to Cloud distance calculation. The suitability of these approaches is also tested.

5.1.1.1 DTM difference

The study of the morphological change in the Charonnier area as a result of the landslide event is carried out by means of subtracting the 1999 DTM from the 1993 DTM.

The 1999 DTM is generated from historical aerial photographs with a resolution of 2400dpi dated in 1999 by means of ERDAS LSP Project manager software. Cell size of the output elevation model is 0.5m and the RMSE is 0.14m. Together with this product, an orthomosaic covering the area in which the two aerial photographs overlap is created (Appendix II).

In figure 5.1, the 1999 DTM shows the elevation of the area surrounding the Charonnier landslide in 1999. The lowest part in the Northeastern corner, with soft green and blue colours, correspond to Le Dreuzt river and its fluvial terrace. Altitude increases towards the Southwest, reaching 1180m in the area adjacent to the crown of the landslide. The framed area delimits the material affected by the event in 1994, around the Charonnier creek valley, which flows towards the Northwest and drains in Le Dreuzet river. Topography in the intersection between the fluvial terrace and the “Terres Noires” is steep, with an altitude increase of 220m in a transect of less than 500m.

Although this elevation model is described as a terrain model, DTM, (displays the elation of the earth surface without the effect of vegetation or buildings), the effect of vegetation is noticeable in the grainy texture displayed in the vegetated areas. LPS Project manager does not classify bare ground and areas covered by vegetation separately, and the terrain extraction is

performed by using all the created tie points as ground elevation information (even though some of them correspond to bushes or trees).

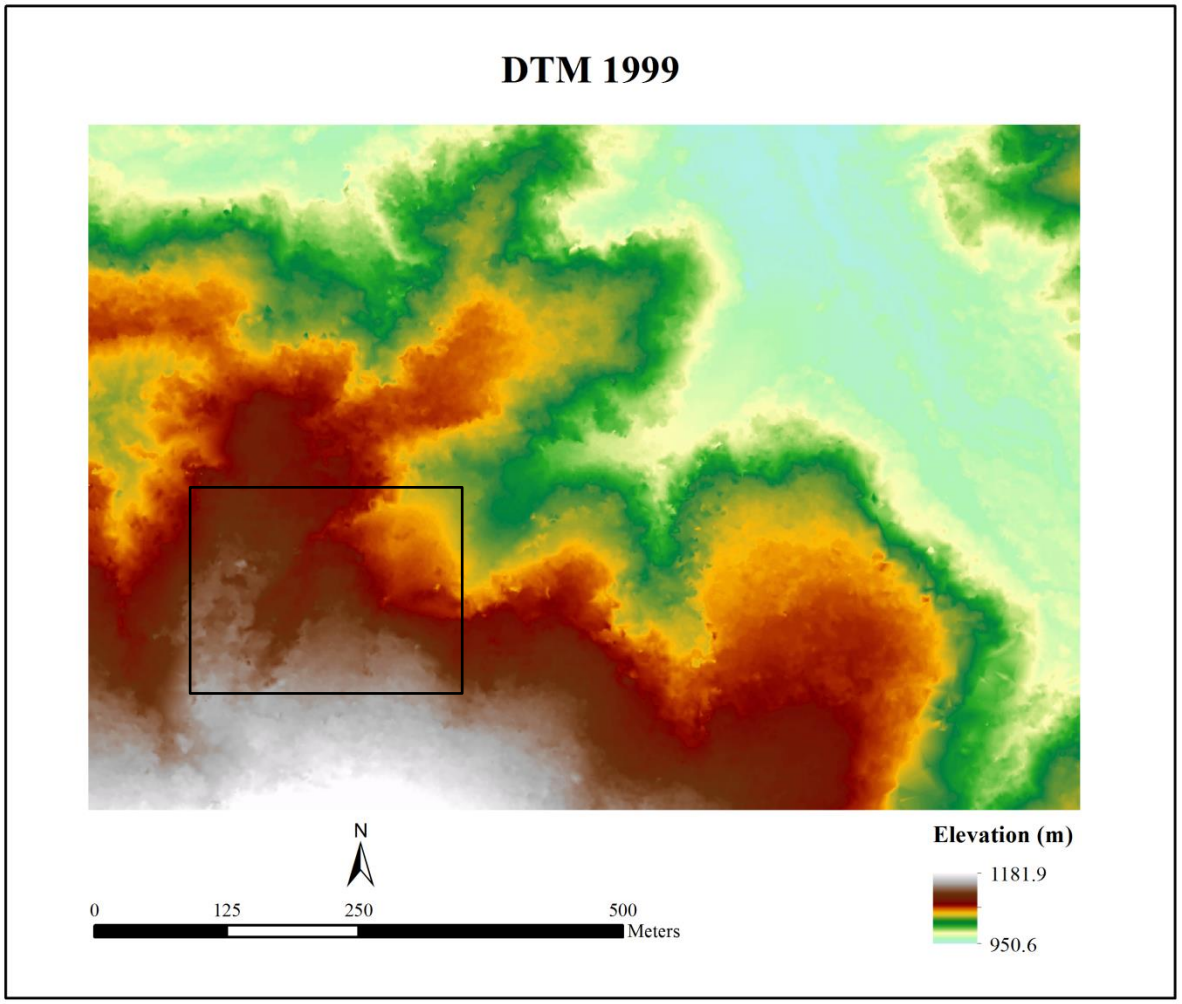

Figure 5.1 Digital Terrain Model of the Charonnier area in 1999, with the landslide location framed by a black rectangle.

1993 DTM (pre-landslide initiation) is available after Van Haaster (2017) (Figure 5.2), with a cell size of 0.5 m and a RMSE of 3.4m, and was created following the same methods as in the 1999 DTM. The orthomosaic resulting from the photogrammetry project can be examined in Appendix I. The visual inspection of the elevation model shows little differences with the 1999 DTM, with the exception of the landslide area, where the original topography (1993) differs from the extracted from 1999 aerial photographs.

The study of the topography change in the landslide location is carried out by means of subtracting the 1999 DEM from the 1993 DEM, bringing, as a result, a raster layer in which the height difference is displayed (figure 5.3). This product illustrates elevation change due to both topographic variation and change in the vegetation cover, with a cell size of 0.5x0.5m.

1994 DEM has a RMSE of 3.4m, so height differences below 3.4m can be linked to the resolution error.

.

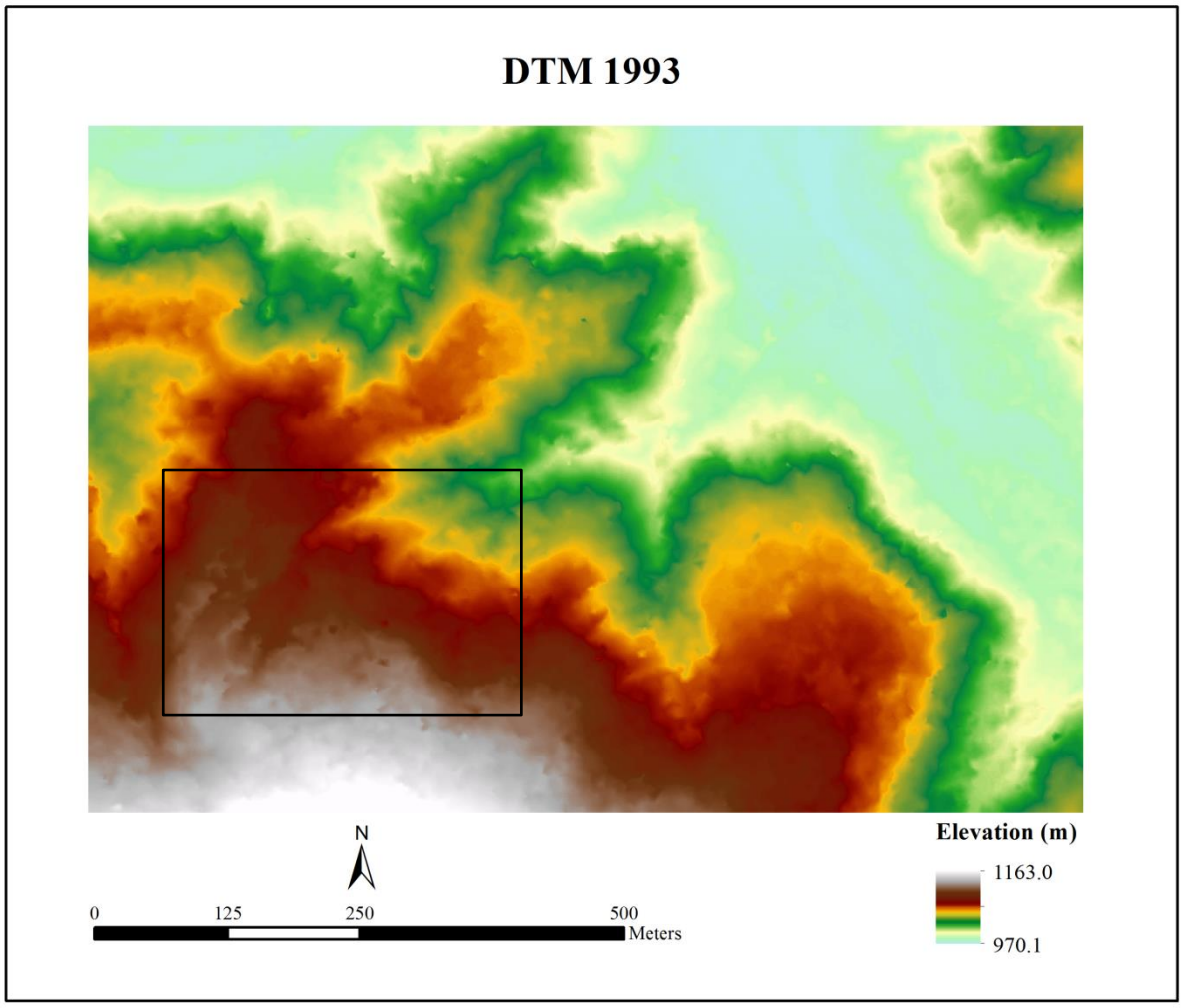

Figure 5.2 Digital Terrain Model of the Charonnier area in 1993, with the landslide location framed by a black rectangle. From (Van Haaster, 2017)

The source area is clearly visible in the centre of figure 5.3, where a continuous and well defined area displays positive values up to 15m surrounded by and area with values close to 0m or negative, meaning an increase in height due to vegetation growth. The map shows a directional trend of elevation change, with the highest values towards the Northeast corner, and the lowest values situated in the Southwest. Although a fraction of the elevation change in the Southwestern part can be linked to vegetation dynamics, this preferential pattern of elevation change cannot be explained by geomorphological processes. These extreme values in opposite corners of the map can be associated to a different choice of settings during the 1993 and 1999 photogrammetry process, leading to a projection offset propagated from an axis crossing the central part of the map in the Northeast-Southwest direction.

The volume of the slumped mass is computed defining a polygon that covers the area with positive values (warm colour pixels) within the framed region in the difference DTM 1993-1999 (Figure 5.3), and it is estimated on 27511.4 ± 10127.1 m^3.

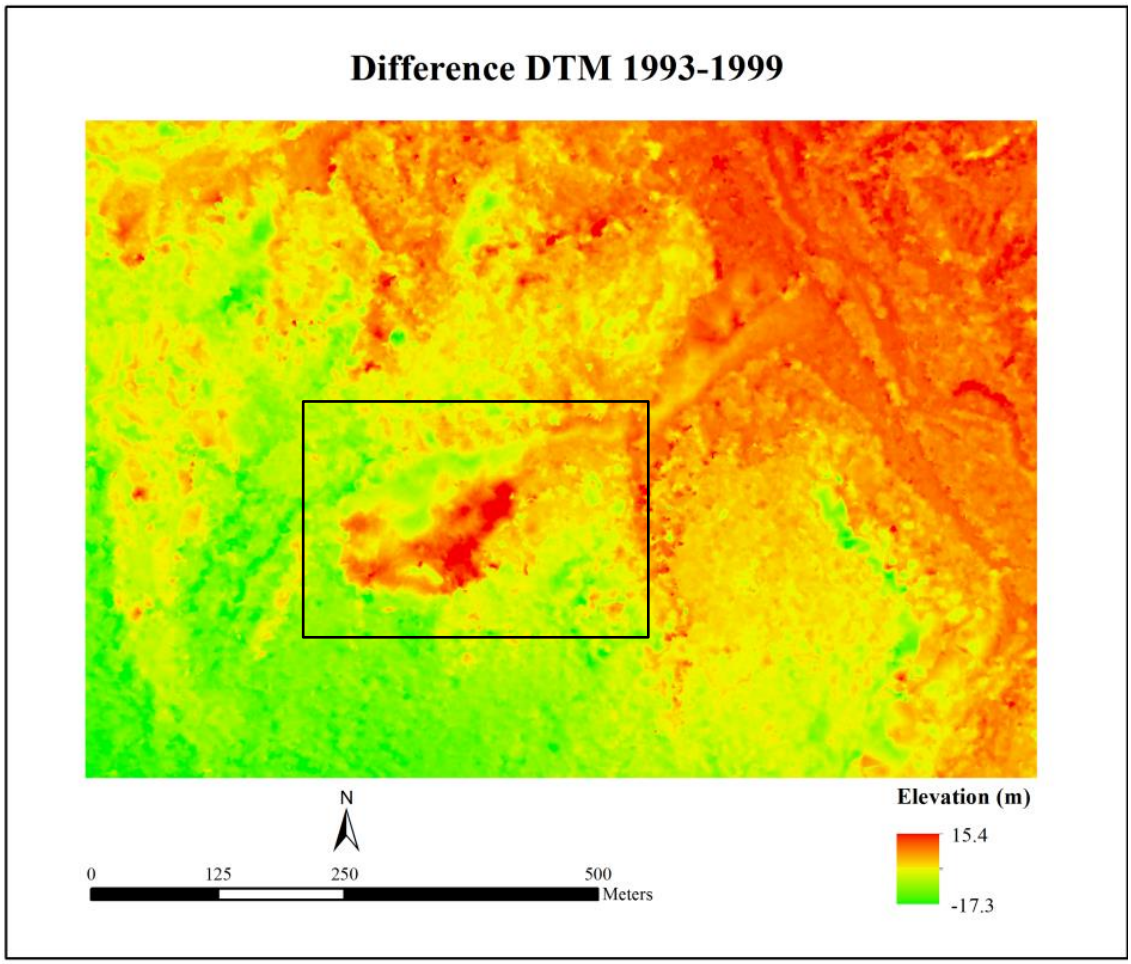

Figure 5.3 Elevation difference at the Charonnier area after subtracting the 1999 DTM from the 1993 DTM. The landslide location is framed by a black rectangle.

5.1.1.2 Cloud to Cloud distance calculation

Dense point clouds (DPC) corresponding to pre and post-landslide initiation are produced through photogrammetry techniques as well.

1993 DPC extends over an area of 26km2 with a point density of 0.2 points/m2, and 1999 DPC has a point density of 0.7 points/ m^2 covering an area of 30km^2.

In this case, the elevation change detection is executed applying the M2C3 algorithm to a section (0.54 km^2) of 1994 and 1999 DPCs, centred at the landslide zone (figure 5.5). The value of the points in the point cloud corresponds to the distance between that point in 1993 and the points in the 1999 DPC calculated as explained in the Methods & Data section. Areas where the point cloud has not been derived in the photogrammetry process due to a lack of tie points appear in white colour.

In the source area, framed by a black rectangle in the derived distance point cloud (figure 5.5), -6.6m and -23.0m are minimum and maximum distance values, with a mean of -11.4m and STD of 5.0m.

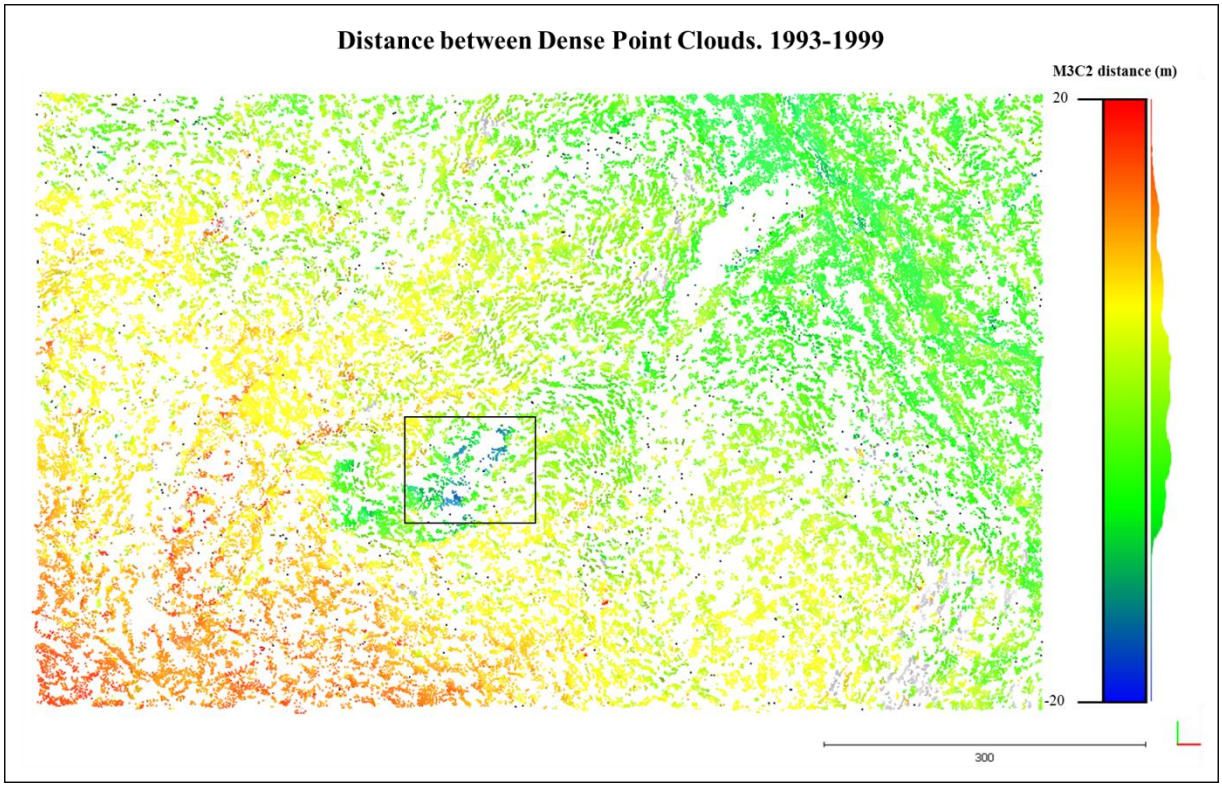

Figure 5.4 Product of the M3C2 algorithm applied in 1993 and 1999 DPC at the Charonnier landslide location.

5.1.1.3 Cloud to Cloud accuracy assessment

DPCs accuracy are assessed jointly after having built the distance map (Figure 5.4). In the control area at the road, the minimum distance between clouds is -1.6m, while the maximum is -8.5m, with a mean of -7.5m and standard deviation of 1.2m. The mean value is taken as vertical error of the final product, so distance values below -7.5m cannot be considered as significant. An area covered by vegetation shows a mean distance between point clouds of 5.3m, ranged between -5.9m and 16.6m, with STD of 4.5m (figure 5.5).

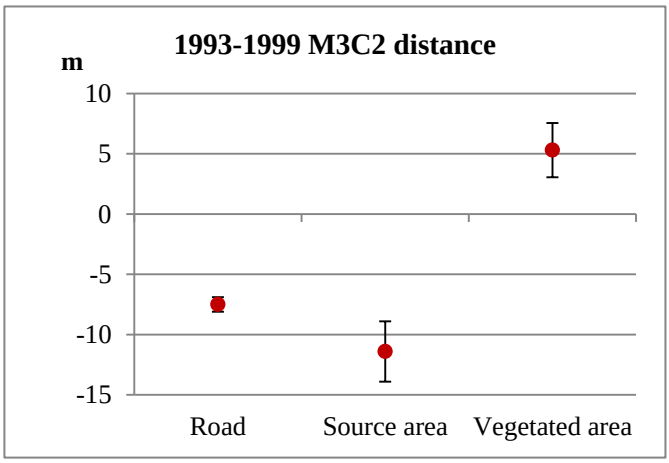

Figure 5.5. Average distance between 1993DPC and 1999DPC computed with M3C2 algorithm at different locations. Vertical bars represent STDV

5.1.2 Landslide dynamics: 2016-2017

The state of the landslide in 2017 in terms of possible dynamism is explored through the use of UAV based pictures.

A DPC, DTM and Orthomosaic are created based on a set of UAV based pictures dated in June 2017 with the SfM algorithm.

5.1.2.1 DTM difference

2017 DTM (Figure 5.6) and Orthomosaic (Figure 5.8) have a resolution of 0.05m and 0.025m respectively, and are georeferenced based on 57 measured GCPs. 2016 DTM is available after Van Haast (2017) and De Vries (2017)

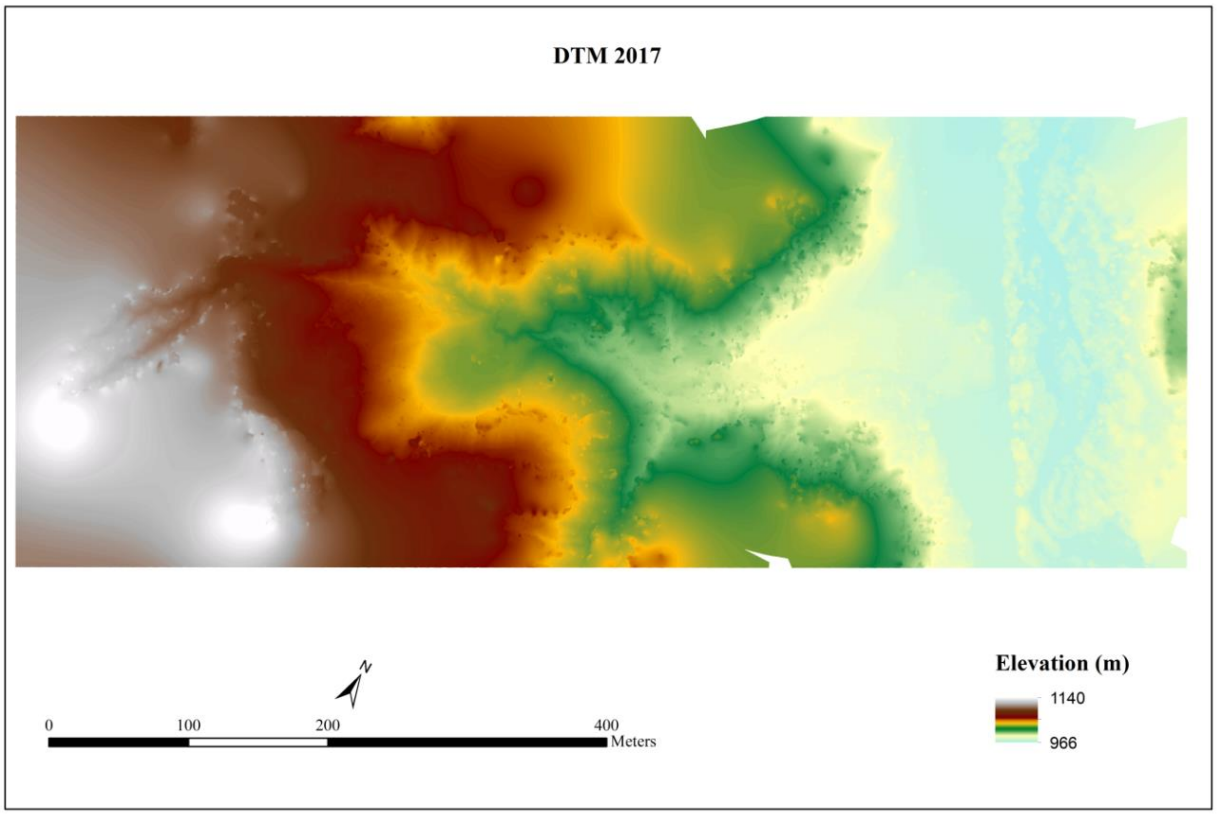

Figure 5.6. DTM of Charonnier landslide (June 2017 survey) derived from SfM

The detection of areas where topographical changes have occurred is carried out by the subtraction of 2017 DTM from 2016 DTM. The resulting raster layer, in figure 5.7, shows the change in elevation as the cell value. The DTMs are created after manually removing the vegetated areas from the Dense Point Clouds. However, some points corresponding to vegetation can remain in the DPC, and affect the quality of the DTM. In the 2017 DTM, the effect of non-deleted vegetation appears in form of discontinuous and granular patches with higher elevation than their surroundings. This effect is also distinguishable in the differential DTM, in which not distinguishable areas exhibit prominent terrain elevation changes; the height differences in the body of the landslide are caused by the difficulty to exclude from the DTM generation all the vegetated areas.

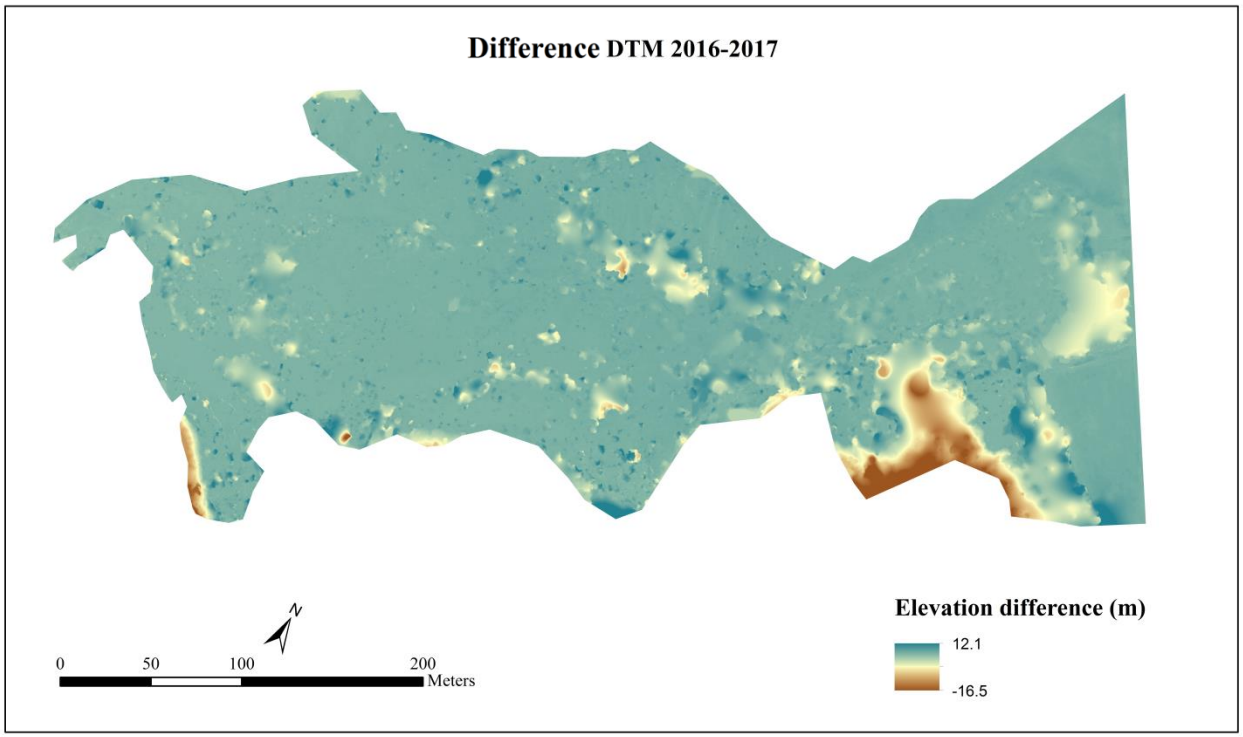

Figure 5.7. Elevation difference map of Charonnier landslide resulting from 2016 DTM and 2017 DTM.

5.1.2.2 2017 DTM Accuracy assessment

The accuracy of the derived 2017DTM is assessed by means of 13 independent 13 GCP (shown in figure 5.8). Overall accuracy is 14cm, and accuracy in the Z direction is 7cm. According to the angle of the positional error, no preferential orientation of the error can be seen (Table 5.1).

Table 5.1. Positional errors in X,Y and Z direction of the DTM 2017. Angle is calculated in the XY directions.

GCP	ΔX(m)	ΔY(m)	ΔZ(m)	Distance(m)	Angle(°)
1	0.00	0.06	0.13	0.14	88.21
3	0.07	0.12	0.09	0.17	300.26
6	0.02	0.07	0.05	0.09	283.65
7	0.06	0.07	0.00	0.09	49.33
12	0.09	0.12	0.18	0.24	51.95
17	0.06	0.00	0.07	0.09	4.69
32	0.10	0.07	0.02	0.12	37.25
39	0.01	0.05	0.01	0.05	74.22
40	0.12	0.06	0.02	0.13	333.43
45	0.04	0.08	0.00	0.09	64.62
54	0.07	0.00	0.03	0.08	3.37
67	0.45	0.05	0.19	0.49	353.60
87	0.03	0.05	0.07	0.10	56.82
	0.09	**0.06**	**0.07**	**0.14**	

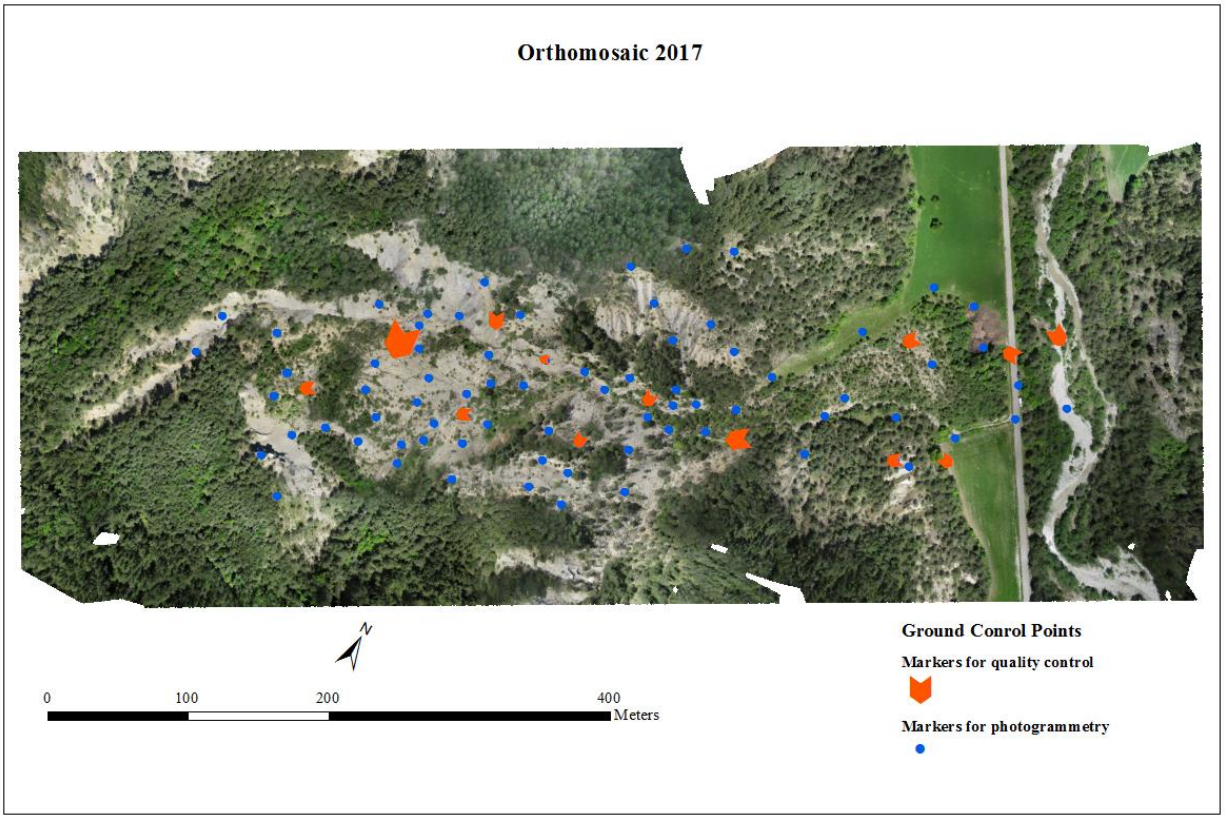

Figure 5.8. Orthomosaic representing the state of Charonnier landslide in June 2017. Location of markers used for the photogrammetry process is displayed as blue points. Markers used for the quality control are displayed as oriented red arrows, whose size depends on the positional error at each location.

5.1.2.3 Cloud to Cloud distance calculation

DPCs corresponding to June 2016 and June 2017, generated with Agisoft Photoscan software, are evaluated with the M2C3 algorithm. Point density, in this case, is greater than in 1993 and 1999 DPCs obtained from historical aerial pictures via ERDAS LPS Project Manager. 2016 DPC covers an area of 0.3 km2, with a point density of 121.1 points/m2. 2017 DPC extends over 0.42 km2 with a density of 128.3 points/m2.

5.1.2.4 Cloud to Cloud accuracy assessment

The comparison between dense point clouds performed by using the M3C2 algorithm in CloudCompare software yield more accurate results than the comparison between DTMs. River incision along the Charonnier creek, and differentiated erosion in the left flank of the creek, where gullies are present can be drown (Figure 5.10). The magnitude of the height change in these areas is bigger than the difference between point clouds in the road. The offset in the road

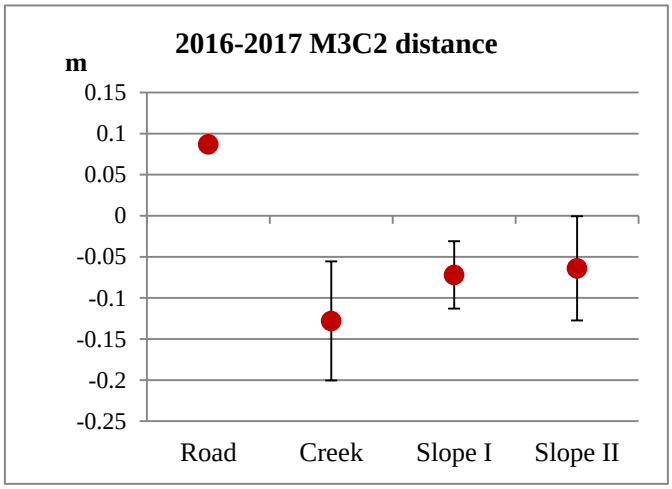

Figure 5.9. Average distance between 2016DPC and 2017DPC computed with M3C2 algorithm at different locations. Vertical bars represent STDV.

location is assumed to represent the vertical accuracy of the point clouds after the photogrammetry process (Figure 5.9).

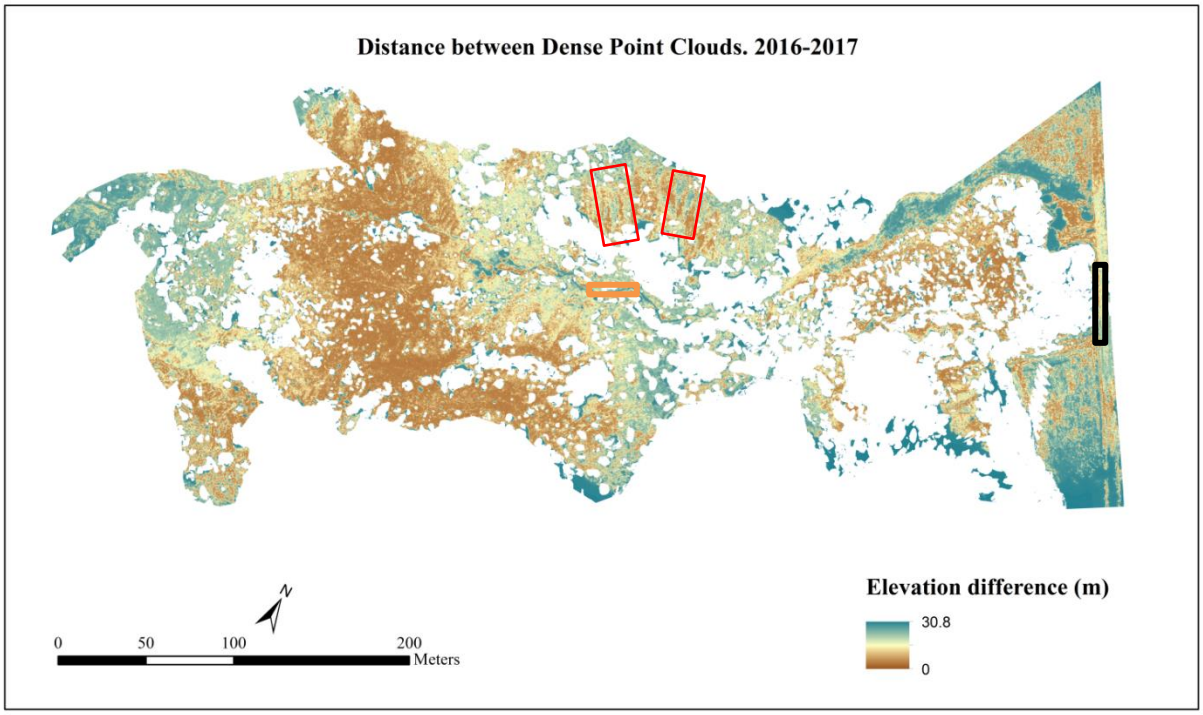

Figure 5.10. Product of the M3C2 algorithm applied in 2016 and 2017 DPC at the Charonnier landslide location. The red rectangles frame the slopes where gullies are present; the reference area at the road is delimited by the black rectangle; and the orange rectangle indicates the part of the creek that has been analysed.

5.1.3 Landslide dynamics between 1999 and 2017

From 1999 to present time geomorphological processes could have affected the landslide. In order to detect them, a differential DTM is created upon 1999 and 2017 DTMs, following the same methodology as the previous analysis. The resulting map (figure 5.11) does not offer very meaningful information *per se* due to the different resolution of the base maps (0.5m in 1999 and 0.05m in 2017) and the detected positional error. Margins of the map show odd values, and offset in the road, assumed to keep a constant elevation, take values up to 5m. However, qualitative interpretation of the resulting differential map, together with on-site visual interpretation of the features of the landslide can trace back processes affecting the landslide. The differential DTM shows granular change patterns outside the core of the landslide linked to the evolution of the vegetation cover, with values up to 10m. Differential erosion can be detected in some sections corresponding to the creek that makes its way along the body of the landslide. Water activity is also detectable in the steep slope in the left flank of the creek, where gullies were observed during the field campaign.

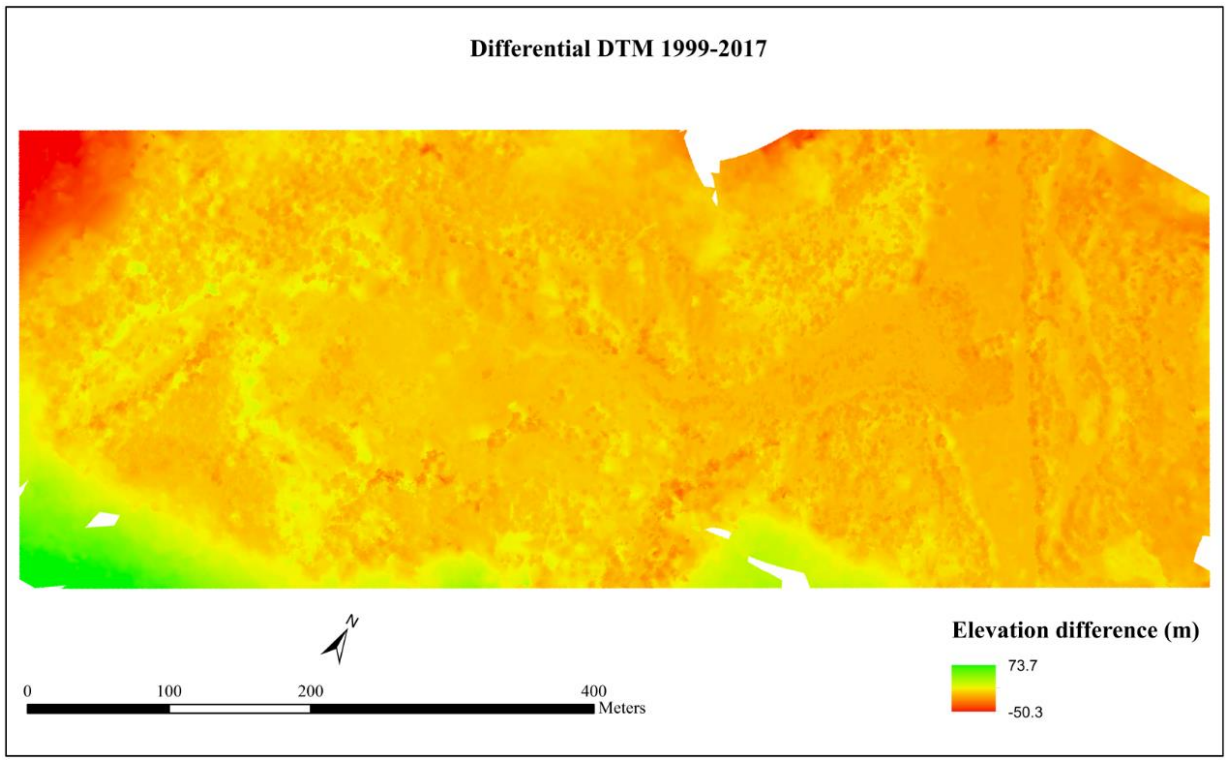

Figure 5.11. Differential map of Charonnier landslide resulting from 1999 DTM and 2017 DTM.

Field observation also suggested possible dynamism in the form of creep in the Eastern part of the scarp of the landslide, where some fallen and bent trees are present as shown in figure 5.12. The material remaining in this section of the scarp show evidences of having been recently exposed, displaying a dark and fresh brown colour, not having been affected yet by weathering. This spot corresponds to small patches on the map displaying negative values up to -7m.

Figure 5.12. Section of the scarp where dynamism has possibly taken place. The blue line delimit the crown; newly exposed, fresh material is shaded in red. Black arrows point to the fallen trees.

A Cloud to Cloud distance calculation with 1999 and 2017 DPC is also performed. In this case, the great difference in point density (0.7 points/ m^2 vs. 128.3 points/m^2) does affect the suitability of the M3C2 algorithm. The computation does not yield any result in some areas (absence of points), and the values of the resulting point cloud do not allow an appropriate analysis (Figure 5.13).

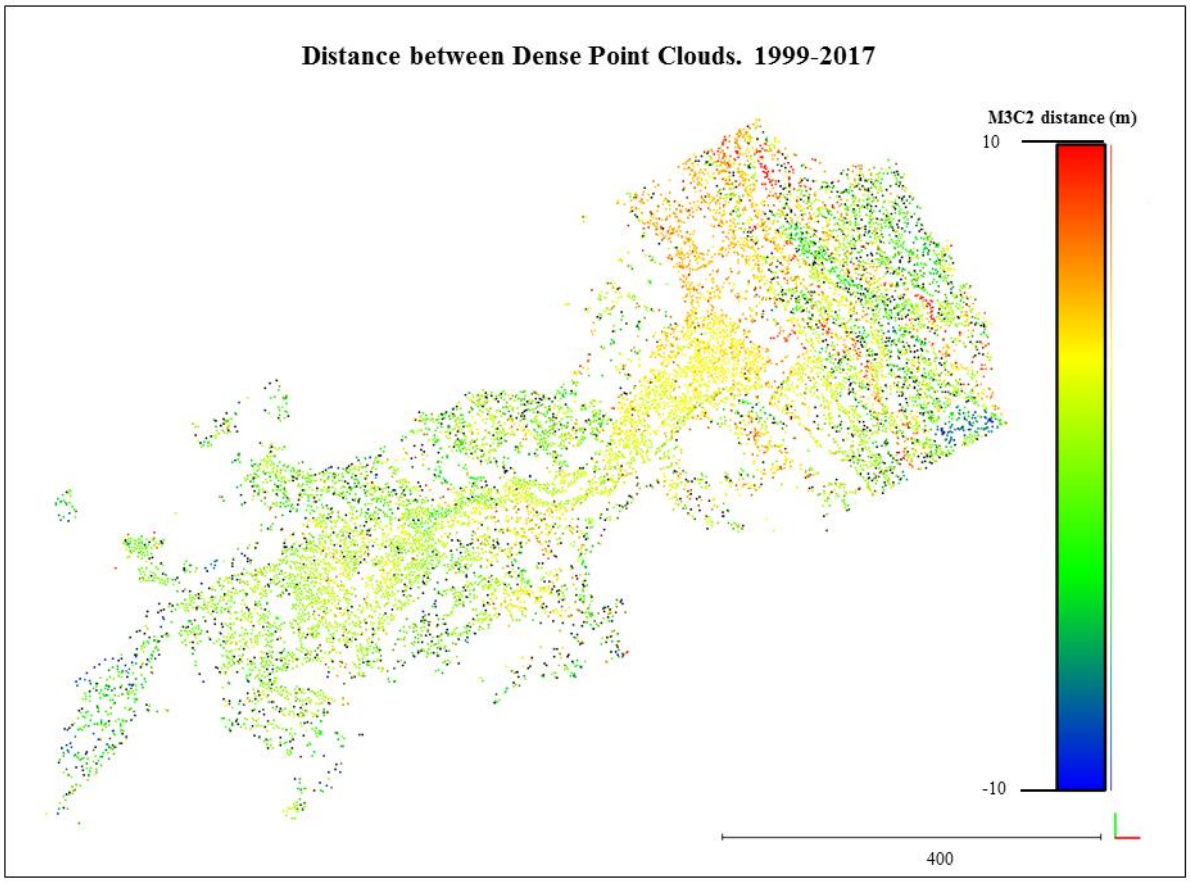

Figure 5.13. Product of the M3C2 algorithm applied in 1993 and 1999 DPC at the Charonnier landslide location.

5.2 Soil characteristics

Characterization of the material of the Charonnier landslide can yield information about temporal or spatial trends in soil properties linked to the development of mass wasting processes or to the dynamics of areas that are already unstable. 29 soil samples were collected during the field campaign in June 2017, 21 of them from the slumped area and 8 from the parent material. 5 conductivity test were perform in-situ (Appendix III).

Additionally to soil samples collected in June 2017, sampled material from the 2016 campaign by De Vries (2017), is also available. This dataset (Appendix IV) offers information about the physical properties of the Charonnier landslide material one year before through the analysis of 36 samples and more than 20 conductivity test.

Table 5.2 includes the statistics of a set of soil properties retrieved after field and laboratory analysis, clustered by the year of sampling and the area of the landslide from where the samples were collected. The inspection of the mean values from 2016 and 2017 sampling campaigns shows comparable results, in the same order of magnitude. Although sampling strategy and sample size are comparable between the 2 years, collection locations and researchers carrying out the sampling process are not the same. Thus, a statistical analysis is required in order to determine whether the mean values from both sampling campaigns are statistically different from each other or not.

Table 5.2. Soil characteristics and statistics from 2016 and 2017 sampling campaigns at Charonnier landslide.

		Dry bulk density [g * cm^{-3}]		VWC [cm3*cm^{-3}]		Porosity [cm3*cm^{-3}]		Conductivity [m^{-1} * d^{-1}]		Field capacity [g /cm^{-3}]		Specific gravity [g * cm^{-3}]		Bulk Weight Saturated [kN * m^{-3}]		Bulk Weight Field capacity [kN * m^{-3}]	
		2016	2017	2016	2017	2016	2017	2016	2017	2016	2017	2016	2017	2016	2017	2016	2017
Slumped	Average	1.53	1.58	0.29	0.20	0.54	0.39	3.49	2.36	0.4	0.39	3.31	2.69	20.28	20.01	18.97	19.73
	STDV	0.1	0.14	0.06	0.05	0.03	0.04	4.2	0.31	0.04	0.05	0.26	0.25	0.95	1.05	1.22	1.10
	n	18	21	18	21	18	14	12	3	18	14	18	14	18	14	18	14
Parent	Average	1.52	1.60	0.31	0.17	0.52	0.41	1.86	0.81	0.41	0.39	3.4	2.70	21.16	19.90	20.31	19.50
	STDV	0.15	0.23	0.05	0.03	0.03	0.07	2.2	0.19	0.04	0.07	0.1	0.24	0.89	1.74	1.04	1.75
	n	18	8	18	8	6	8	10	2	6	8	6	8	6	8	6	8
Total	Average	1.53	1.59	0.38	0.19	0.53	0.40	2.6	1.74	0.41	0.39	3.33	2.69	20.5	19.97	19.31	19.65
	STDV	0.13	0.17	0.05	0.05	0.03	0.06	3.2	0.80	0.44	0.06	0.23	0.25	0.97	1.35	1.27	1.38
	n	36	29	36	29	24	22	22	5	24	22	24	22	24	22	24	22

After the performance of the t-test, only for the VWC the null hypothesis can be rejected, for both parent and slumped material, and be established that the difference between means are significant: it can be stated form the collected samples than water content of the landslide material is higher on June 2016 than on June 2017.

For none of the other tested parameters the null hypothesis can be rejected so, at a 95 confidence level, differences between means are not significant. Given that it cannot be proved that soil properties (DBD, conductivity, field capacity, specific gravity, saturated bulk weight and bulk weight at field capacity) have variated within the last year, 2016 and 2017 samples are pooled to infer the statistical significance of the difference of soil properties between the accumulated and the source area applying, as above, a t-test. The results of the statistical test conclude that there is not a significant difference in the soil properties between the source and the accumulation area.

6. Discussion

The landslide that was initiated in February 1994, affecting materials in the small valley created by the Charonnier river, does not present motion or deformation caused by a reactivation of the slope process as it can be detected by analysing historical aerial photographs and UAV based imagery. However, the combined use of remote sensing, photogrammetry and geospatial formats detects erosion and gully incision, as secondary processes, acting on the landslide surface.

6.1 Remote sensing, photogrammetry and GIS

The investigation of the dynamics of the landslide through remote sensing appears as a cost-efficient approach that can offer profitable results.

From a stereoscopic pair from 1999 that covers the area around the Charnnier landslide, a photogrammetry process is performed with the help of ERDAS LPS Project Manager software. The pair of input images is scanned with a resolution of 2400dpi, and the camera report for that flight is also available, allowing the production of a DTM and orthomosaic with a cell size of 0.5m and RMSE of 0.14m. Van Haaster (2017) also obtained a DTM and orthomosaic of the Charonnier landslide in 1999 using the same stereoscopic pair as input, but with a lower resolution, which decreased the quality of the outputs (RMSE of 3.38m). Van Haaster (2017) derived the 1993 DTM from aerial pictures with a resolution of 900dpi and without a camera report that would have provided the interior orientation parameters. RMSE of this products, with a resolution of 0.5m, was 3.52m.

Topographic information in raster format (DEM) for 1999 is subtracted from 1993 DEM, generating a differential DEM in raster format. Even though the magnitude of combined error is noteworthy (3.4m), topographic changes in the area affected by the landslide in 1994 are bigger than that. Subsequently, the location where elevation has decreased can be identified as the area where mass has depleted. The volume of the mobilized material can be calculated with ArcGIS software in a pixel per pixel basis, as the value of the cell times its spatial coverage ($0.25m^2$). The use of new 1999DEM, generated from 2400dpi imagery, leads to a slightly different differential map and volume calculation, still within the range proposed by Van Haaster (2017) of 21,600 m^3 $\pm$ 52,400.

Photogrammetry processes carried out with the aforementioned software can also produce Dense Point Clouds, representing the topography of the area under study. M3C2 algorithm included in CloudCompare program calculates the distance between point clouds. Initially thought to be used with LIDAR data (Cook, 2017; James et al., 2017; Lague et al., 2013), with homogeneous point spacing, this algorithm can also offer quality results if parameters are adjusted. With this new approach for topographical change detection, distances are calculated between 1993 and 1999, 2016 and 2017, and 1999 and 2017 DPCs. *Normal, projection* and *subsampling* settings were tweaked separately for each comparison, given that point density is notably greater at DPCs created through Agisoft Photoscan than through ERDAS IMAGINE. Accuracy in the 1993-1999 DPCs distance calculation is lower than in the 2016-2017 case, still sufficient to detect the material mobilized in February 1994. 2016-2017 DPCs distance calculation also detects the differential erosion caused by runoff, along the Charonnier creek and

on the north-west slope, where gullies keep incising into the Terre Noires, with elevation changes up to 12cm.

However, the use of the M3C2 algorithm with 1999 and 2017 DPCs does not offer meaningful results, probably due to their disparate point density.

6.2 Soil characterization

The Charonnier landslide has been subject of study only from June 2016, although the initiation of the mass wasting process took place in January 1994 after an extreme and prolonged wet period. Thus, soil characteristics at the time of the event are not available and cannot be included in stability models aimed to reconstruct the causes of the failure (De Vries, 2017).

Nevertheless, it is convenient to compare soil parameters retrieved with one year span (June 2016 and June 2017) in order to assess the current short-term dynamics at the landslide location. Sampling techniques and soil analysis in June 2017 was pretended to be analogous to June 2016 data processing. Still, last sample size is slightly smaller than in 2016 due to difficulty to perforate the soil and collect the cores given the dryness of the material.

For all the inferred parameters from 2017 sampling campaign, values are comparable to 2016 campaign and other studies focused on locations where the presence of Terres Noires defines the lithology (Antoine et al., 1995a; Malet et al., 2005; Maquaire et al., 2003).

The results from t-test reveal that there is not statistically significant difference between 2016 and 2017 soil parameters and between parent and slumped material. The only parameter that shows a significant variance between years is soil moisture, characteristic highly dependent on dry or wet events (Van Asch et al., 1999). In June 2017, soil water content is lower than in the previous year, as it could be qualitatively inferred during the field campaign.

7. Conclusions

The development of Unmanned Aerial Vehicles (UAV) and photogrammetry techniques bring researchers a new tool for earth observations and geomorphological studies. This research aims to prove that the combination of airborne imagery (UAV and historical flights) processed via different photogrammetry programs can produce quality products in form of Digital Elevation Models, orthomosaics and Dense Point Clouds, which can be used in the reconstruction of landslide events, the analysis of their stability and the detection possible hazards

7.1 Research questions

The dynamics affecting Charonnier landslide can be detected from historical aerial pictures when the magnitude of the change is on a large scale. Pairs of stereo images from 1993 and 1999 allow the detection and volume estimation of the mass movement in January 1994, since terrain sank up to 15m in the source area of the landslide.

The enhancement of the resolution of the aerial pictures used as input improves significantly the photogrammetry process, reducing the RMSE one order of magnitude.

Comparison of 2016 and 2017 DTMs, generated from UAV based imagery, ensure that Charonnier landslide has not been reactivated in the last year. However, erosion processes do act on the flanks of Charonnier creek, where gullies have incised between 5 and 10cm from 2016 to 2017. The bed of the creek itself has been also cut into the material around 12cm in some locations.

The detection of erosive activity in a steep location as the Charonnier landslide hillslopes as a secondary process is not possible through DTM subtraction. This technique cannot overcome the limitation of height changes in steep slopes, and spatial resolution may be insufficient. DPC distance calculation with the M3C2 algorithm requires a trial-error process to adjust the parameters, plus really computationally intensive, but gives results that show erosion effects within centimetres.

This new methodology of Point Cloud is more often used with LIDAR point clouds (high density, regular clouds) but can also be applied with point clouds resulting from photogrammetry, and yields more detailed results for the scale of erosion process. Nevertheless, point density and the magnitude of the detectable elevation change are inversely proportional. Furthermore, following this case study, it has been noticed that point cloud distance calculation depends on the availability of DPC with similar point density; otherwise, M3C2 algorithm results are not conclusive in some areas of the surveyed location.

Soil parameterization over two consecutive years is performed with the help of two field campaigns of soil sampling, with analogous strategy. Results of the analyses do not give rise to temporal or spatial statistically significant differences. Volume of the sampled material is limited by the steepness of some locations on the body of the landslide, the presence of vegetation and the use of manual tools. Volume of water required for the conductivity tests is much higher than the volume that can be collected and manually transport from the Charonnier creek.

7.2 Recommendations

Photogrammetry projects from historical aerial pictures carried out with LPS Project Manager from ERDAS require the availability of a set of parameters in order to build the interior orientation. This information is collected on the camera report corresponding to the flight campaign. l'Institut national de l'information géographique et forestière (IGN) offers access to a catalogue of aerial photographs that cover the French territories from 1919, but does not supply the camera reports of the flights. The absence of this material hampers the achievement of high accuracy topographic models, because interior orientation parameters have to be manually derived, adding a source of error to the photogrammetry process.

As it has been proven in the results chapter, the availability of high resolution scanned photographs would also permit better results from the photogrammetry process. IGN images are only provided in .jp2000 format and with coarse resolution (900 dpi maximum), which is very limited for their further processing.

If high quality photographs and the interior orientation parameters were available, elevation information for almost 100 years could be reconstructed with high accuracy for morphodynamic studies or other geophysical surveys.

Regarding the UAV campaign, the availability of an on-board GPS would enhance the accuracy of the SfM technique, adding camera orientation information. An improvement of the resolution of the camera would also help in the photogrammetry process in Agisoft Photoscan. This way, the number or required GCP would be lower, involving less human resources in the process of placing the markers on the study site, while the accuracy of the products would be higher, allowing for the detection of elevation changes in the order of few centimetres.

The soil sampling campaign could be more extensive if the availability of water and time rises, as well as if mechanical drilling tools are used. With a bigger soil sample size, spatial patterns in soil characteristics and conclusive differences between dates could be significant.

This data could be incorporated in spatial distributed stability models which aim to reconstruct the mechanisms that triggered the landslide or the risk of reactivation. However, the cost-effectiveness of this campaign should be analysed.

The study of the dynamic of the landslide can be also complemented with a geotechnical approach. The installation of inclinometers can detect small terrain movements, and mechanical drilling could help in the detection of the water table and failure surface detection. These two important features can also be inferred by means of Electrical Resistivity Tomography (ERT) profiles.

8. References

Agisoft. (2017). PhotoScan professional 1.4.2 user manual. St. Petersburg.

Antoine, P., Giraud, A., Meunier, M., & Van Asch, T. (1995a). Geological and geotechnical properties of the "Terres Noires" in southeastern France: Weathering, erosion, solid transport and instability. *Engineering Geology*, *40*(3–4), 223–234.

Antoine, P., Giraud, A., Meunier, M., & Van Asch, T. (1995b). Geological and geotechnical properties of the "Terres Noires" in southeastern France: Weathering, erosion, solid transport and instability. *Engineering Geology*, *40*(3–4), 223–234.

Ayala, F., & Ferrer, M. (1989). Extent and economic significance of landslides in Spain. In *Proceedings of the 28th International Geological Congress: Symposium on landslides* (pp. 169–178). Washington , DC.

Bogaard, T. (2001). Analysis of hydrological processes in unstable clayey slopes. *Nederlandse Geografische Studies*, (287).

Bogaard, T. A., & Greco, R. (2016). Landslide hydrology: from hydrology to pore pressure. *WIREs Water*, *3*, 439–459.

Busker, T. (2017). *A new methodology for measuring ice cliff backwasting rates on debris-covered glaciers using high-resolution unmanned aerial vehicle imagery*. Utrecht University.

Cammeraat, L. H., van Beek, L. P. H., & Dorren, L. K. A. (2001). Eco-Slopes. Field Protocol. *Eco-Engineering and Conservation of Slopes for Long-Term Protection from Erosion, Landslides and Storms*.

Caris, J. P. T., & Asch, T. W. J. Van. (1991). Geophysical, geotechnical and hydrological investigations of a small landslide in the French Alps. *Engineering Geology*, *31*, 249–276.

Caris, J. P. T., & Van Asch, T. W. J. (1991). Geophysical, geotechnical and hydrological investigations of a small landslide in the French Alps. *Engineering Geology*, *31*(3–4), 249–276.

Casale, R., Fantechi, R., & Flageollet, J. (1993). *The temporal occurrence and forecasting of landslides in the European Community*.

Castellanos Abella, E. a. (2008). *Multi-scale landslide risk assessment in Cuba*.

Colesanti, C., & Wasowski, J. (2006). Investigating landslides with space-borne Synthetic Aperture Radar (SAR) interferometry. *Engineering Geology*, *88*(3–4), 173–199.

Cook, K. L. (2017). An evaluation of the effectiveness of low-cost UAVs and structure from motion for geomorphic change detection.

Cook, K. L., & L., K. (2017). An evaluation of the effectiveness of low-cost UAVs and structure from motion for geomorphic change detection. *Geomorphology*, *278*, 195–208.

Cruden, D. M., & Varnes, D. J. (1996). Landslide Types and Processes. In *Special Report* (pp. 36–75). Edmonton, Alberta: Transportation Research Board, National Academy of Sciences.

De Jong, S. M., Addink, E., & Heuff, F. (2015). *Remote Sensing: a tool for environmental observations*. *Utrecht University*. Utrecht.

De Vries, J. (2017). *Landslide stability analysis using UAV remote sensing and in situ observations*. Utrecht University.

Descroix, L., & Gautier, E. (2002). Water erosion in the southern French alps: climatic and human mechanisms. *CATENA*, *50*(1), 53–85.

Descroix, L., & Mathys, N. (2003). Processes, spatio-temporal factors and measurements of current erosion in the French Southern Alps : a review. *Earth Surf. Process. Landforms Process. Landforms*, *28*(28), 993–1011.

Dewitte, O., Jasselette, J.-C., Cornet, Y., Van Den Eeckhaut, M., Collignon, A., Poesen, J., & Demoulin, A. (2008). Tracking landslide displacements by multi-temporal DTMs: A combined aerial stereophotogrammetric and LIDAR approach in western Belgium. *Engineering Geology*, *99*, 11–22.

Dikau, R., Brunsden, D., Schrott, L., & Ibsen, M.-L. (1996). *Landslide recognition : identification, movement, and causes*. Wiley.

Embleton and Thornes (Ed.). (1979). *Process in geomorphology*. London: Edward Arnold.

ERDAS. (2008). LPS Automatic Terrain Extraction. User's Guide.

ERDAS. (2010). LPS Project Manager. User's Guide.
Gibson, P. J. (Paul J., & Power, C. H. (2000). *Introductory remote sensing : principles and concepts*.
Guha-Sapir, D. (2017). *EM-DAT: The Emergency Events Database*. Brussels, Belgium.
Guzzetti, F. (2000a). Landslide fatalities and the evaluation of landslide risk in Italy. *Engineering Geology*, *58*, 89–107. Retrieved from www.elsevier.nl/locate/enggeo
Guzzetti, F. (2000b). Landslide fatalities and the evaluation of landslide risk in Italy. *Engineering Geology*, *58*(2), 89–107.
Hearn, G. J., & Hart, A. B. (2011). Chapter Five Geomorphological Contributions to Landslide Risk Assessment Theory and Practice.
Huggel, C., Salzmann, N., Allen, S., Caplan-Auerbach, J., Fischer, L., Haeberli, W., … Wessels, A. R. (2010). Recent and future warm extreme events and high-mountain slope stability. *Phil. Trans. R. Soc. A*, *368*, 2435–2459.
Immerzeel, W. W., Kraaijenbrink, A., Shea, J. M., Shrestha, A. B., Pellicciotti, F., Bierkens, M. F. P., & De Jong, S. M. (2014). High-resolution monitoring of Himalayan glacier dynamics using unmanned aerial vehicles. *Remote Sensing of Environment*, *150*, 93–103.
James, M. R., Robson, S., & Smith, M. W. (2017). 3-D uncertainty-based topographic change detection with structure-from-motion photogrammetry: precision maps for ground control and directly georeferenced surveys. *Earth Surface Processes and Landforms*, *42*(12), 1769–1788.
Kappes, M. S., Malet, J.-P., Rematre, A., Horton, P., Jaboyedoff, M., & Bell, R. (2011). Assessment of debris-flow susceptibility at medium-scale in the Barcelonnette Basin, France. *Nat. Hazards Earth Syst. Sci*, *11*, 627–641.
Kjekstad, O., & Highland, L. (2009). Economic and Social Impacts of Landslides. In Kyoji Sassa & Paolo Canuti (Eds.), *Landslides – Disaster Risk Reduction* (pp. 573–587). Berlin: Springer.
Konecny, G. (2003). *Geoinformation: remote sensing, photogrammetry and geographic information systems*. London: Taylor & Francis.
Lague, D., Brodu, N., & Leroux, J. (2013). Accurate 3D comparison of complex topography with terrestrial laser scanner: Application to the Rangitikei canyon (N-Z). *ISPRS Journal of Photogrammetry and Remote Sensing*, *82*, 10–26.
Legg, C. (1994). *Remote sensing and geographic information systems : geological mapping, mineral exploration and mining*. John Wiley & Sons.
Lillesand, T. M., Kiefer, R. W., & Chipman, J. W. (2015). *Remote sensing and image interpretation*. Wiley.
Lu, N., & Godt, J. W. (2013). *Hillslope hydrology and stability*. Cambridge University Press.
Lucieer, A., De Jong, S. M., & Turner, D. (2014). Mapping landslide displacements using Structure from Motion (SfM) and image correlation of multi-temporal UAV photography.
Malet, J.-P., Van Asch, T. W. J., Van Beek, R., & Maquaire, O. (2005). Forecasting the behaviour of complex landslides with a spatially distributed hydrological model. *Natural Hazards and Earth System Sciences*, *5*, 71–85.
Maquaire, O., Malet, J.-P., Remaître, A., Locat, J., Klotz, S., & Guillon, J. (2003). Instability conditions of marly hillslopes: towards landsliding or gullying? The case of the Barcelonnette Basin, South East France. *Engineering Geology*, *70*(1), 109–130.
Metternicht, G., Hurni, L., & Gogu, R. (2005). Remote sensing of landslides: An analysis of the potential contribution to geo-spatial systems for hazard assessment in mountainous environments. *Remote Sensing of Environment*, *98*(2), 284–303.
Niebergall, S., Loew, A., & Mauser, W. (2007). Object-Oriented Analysis of Very High-Resolution. QuickBird Data for Mega City Research in Delhi/India. *Urban Remote Sensing Joint Event* .
Pech, P., & Sevestre, A. (1994). Les Conséquences Financières de L'Épisode Pluvieux Dans Le Bassin-Versant Du Buëch. *Mappemonde*, *4*.
Schuster, R. L., & Fleming, R. W. (1986). Economic Losses and Fatalities Due to Landslides. *Environmental & Engineering Geoscience*, *xxiii*(1).
Selby, M. J. (1993). *Hillslope materials and processes*. Oxford University Press.
Skempton, A. W., & Delory, F. A. (1957). Stability of Natural Slopes in London Clay. In *4th Intern. Conf. Soil Mech. Foundation Eng* (pp. 351–378). London.

Smith, M. W., Carrivick, J. L., & Quincey, D. J. (2016). Structure from motion photogrammetry in physical geography. *Progress in Physical Geography*, *40*(2).
Star, J., & Estes, J. (1990). *Geographic Information Systems: An Introduction*. New Jersey: Prentice Hall.
Swiss Re. (2017). *Natural catastrophes and man-made disasters in 2016: a year of widespread damages Executive summary*.
Turner, D., Lucieer, A., & de Jong, S. M. (2015). Time series analysis of landslide dynamics using an Unmanned Aerial Vehicle (UAV). *Remote Sensing*.
USGS. (2004). *Landslide Types and Processes*.
Van Asch, T. W. J., Beek, L. P. H. Van, & Bogaard, T. A. (2007). Problems in predicting the mobility of slow-moving landslides. *Engineering Geology*, (91), 46–55.
Van Asch, T. W. J., Buma, J., & Van Beek, L. P. H. (1999). A view on some hydrological triggering systems in landslides. *Geomorphology*, *30*(1–2), 25–32.
Van Asch, W. T., Van Beek, L. P. ., & Bogaard, T. A. (2009). The diversity in hydrological triggering systems of landslides. In *First Italian Workshop on Landslides* (pp. 8–10).
van Beek, L. P. H. (2003). Assessment of the influence of changes in land use and climate on landslide activity in a Mediterranean environment. *Nederlandse Geografische Studies*, (294).
Van Haaster, S. (2017). *Photogrammetry and in situ observations to produce high detailed geo-information of the Charonnier landslide*. Utrecht University.
Varnes, D. J. (1978). Slope Movement Types and Processes. In *Landslides—Analysis and control* (pp. 11–33). Washington, D.C.: National Research Council, Transportation Research Board.
Varnes, D. J. (David J., & International Association of Engineering Geology (IAEG). (1984). *Landslide hazard zonation : a review of principles and practice*. *Natural Hazards*. Paris: UNESCO.
Westoby, M. J., Brasington, J., Glasser, N. F., Hambrey, M. J., & Reynolds, J. M. (2012). "Structure-from-Motion" photogrammetry: A low-cost, effective tool for geoscience applications. *Geomorphology*, *179*, 300–314.
Wieczorek, G. F. (1996). Landslide triggering mechanisms. *Special Report - National Research Council, Transportation Research Board*, *247*, 76–90.

9. Appendix

I. Orthomosaic resulting from the photogrammetry processes in LPS Manager. 1993

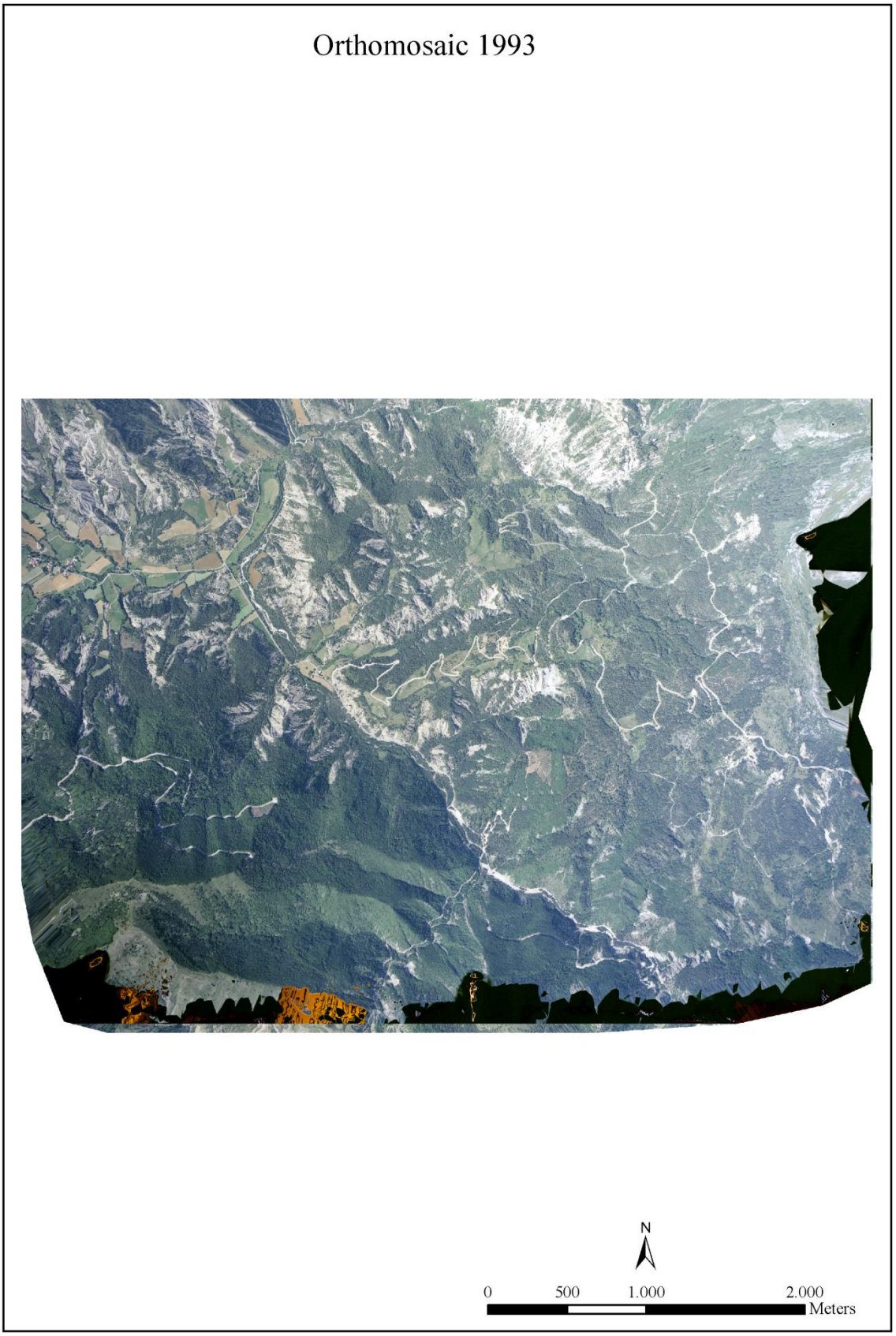

II. Orthomosaic resulting from the photogrammetry processes in LPS Manager. 1999 and used GPC.

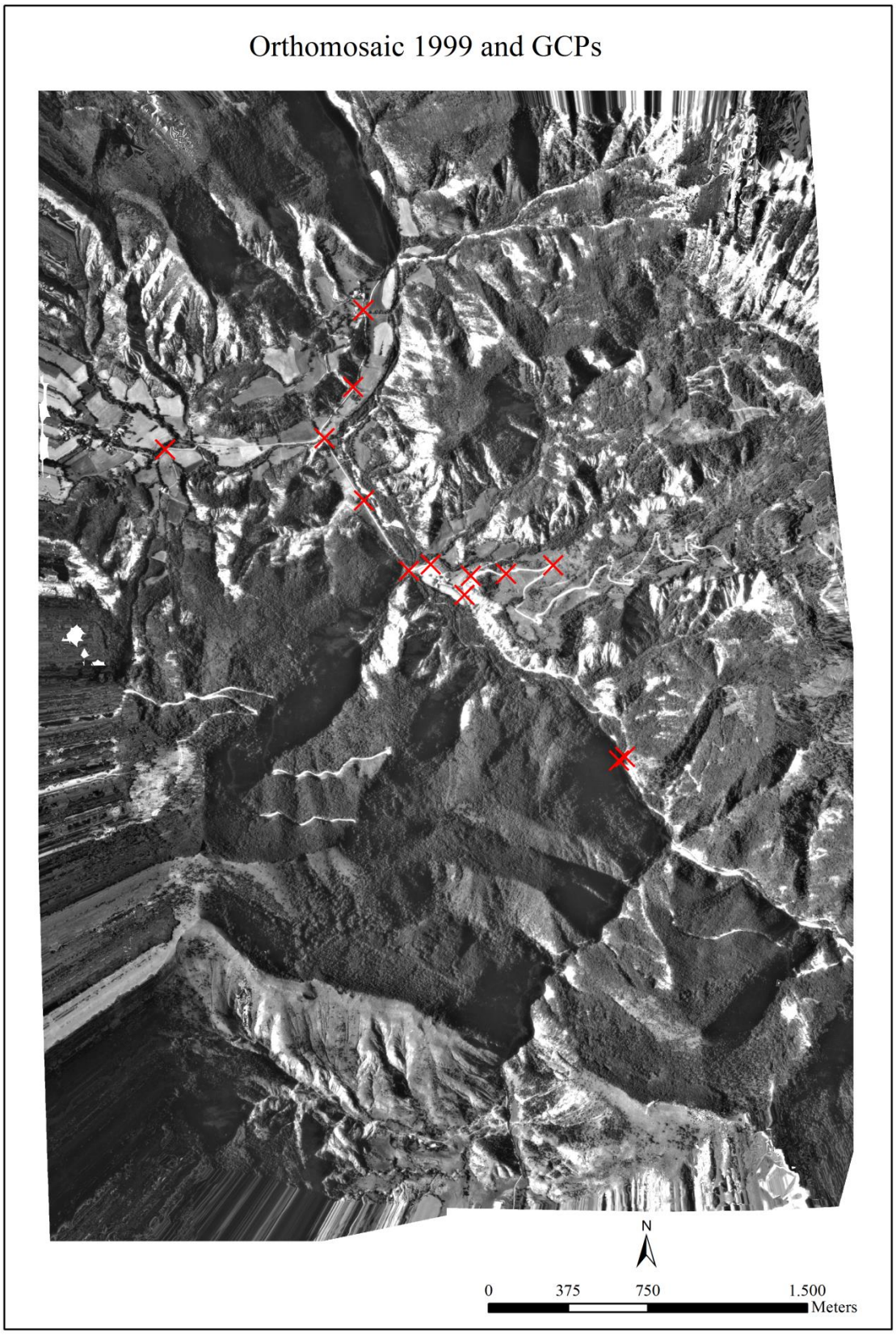

III. Soil samples 2017

Sample code	Location	Depth	Dry bulk density	VWC	Porosity	Conductivity	Field capacity	Specific gravity	Saturated Bulk Weight		Bulk Weight at Field capacity	
		[cm]	[g * cm^{-3}]	[$cm3*cm^{-3}$]	[$cm3*cm^{-3}$]	[$m-1 * d^{-1}$]	[$cm3 *cm^{-3}$]	[g * cm^{-3}]	[kN * m^{-3}]	[g * cm^{-3}]	[kN * cm^{-3}]	[g * cm^{-3}]
S01	Slumped	20	1.56	0.22	-	-	-	-	-	-	-	
S03	Slumped	57	1.55	0.14	0.35	-	0.342	2.39	18.94	1.93	18.58	1.90
S04	Slumped	55	1.53	0.14	-	-	-	-	-	-	-	-
S05	Slumped	45	1.61	0.11	0.30	-	0.279	2.30	18.94	1.93	18.50	1.89
S06	Slumped	72	1.76	0.23	0.37	-	0.356	2.77	20.97	2.14	20.68	2.11
S09	Slumped	77	1.63	0.20	0.36	2.26	0.352	2.55	19.70	2.01	19.43	1.98
S10	Slumped	69	1.34	0.15	0.41	-	0.394	2.26	17.50	1.79	17.11	1.75
S11	Slumped	53	1.25	0.14	-	-	-	-	-	-	-	-
S14	Slumped	57	1.71	0.25	0.37	-	0.379	2.73	20.52	2.09	20.38	2.08
S15	Slumped	49	1.80	0.18	-	-	-	-	-	-	-	-
S16	Slumped	50	1.54	0.19	-	-	-	-	-	-	-	-
S27	Slumped	62	1.57	0.18	0.38	-	0.369	2.55	19.40	1.98	19.08	1.95
S28	Slumped	54	1.60	0.21	0.41	2.04	0.417	2.72	19.86	2.03	19.72	2.01
S29	Slumped	40	1.46	0.24	-	-	-	-	-	-	-	-
S30	Slumped	55	1.68	0.14	0.35	-	0.334	2.59	20.00	2.04	19.66	2.01
S32	Slumped	56	1.33	0.15	-	-	-	-	-	-	-	-

S34	Slumped	55	1.59	0.24	0.47	-	0.455	2.99	20.43	2.08	20.08	2.05
S35	Slumped	40	1.60	0.27	0.44	2.77	0.454	2.85	20.19	2.06	20.09	2.05
S36	Slumped	42	1.76	0.28	0.43	-	0.436	3.08	21.64	2.21	21.41	2.18
S37	Slumped	32	1.64	0.23	0.45	-	0.447	2.97	20.61	2.10	20.43	2.08
S39	Slumped	40	1.77	0.23	0.40	-	0.394	2.96	21.42	2.19	21.09	2.15
S12	Parent	40	1.81	0.13	0.35	-	0.326	2.81	21.43	2.19	20.87	2.13
S13	Parent	32	1.46	0.13	0.33	-	0.339	2.19	17.91	1.83	17.71	1.81
S17	Parent	10	-	-	-	1.01	-	-	-	-	-	-
S19	Parent	10	-	-	-	0.62	-	-	-	-	-	-
S40	Parent	23	1.79	0.22	0.40	-	0.398	2.97	21.71	2.22	21.44	2.19
S41	Parent	13	1.43	0.16	0.50	-	0.485	2.89	19.44	1.98	18.90	1.93
S43	Parent	47	1.85	0.21	0.36	-	0.358	2.89	21.89	2.23	21.61	2.21
S44	Parent	41	1.79	0.19	0.34	-	0.318	2.73	21.06	2.15	20.59	2.10
S46	Parent	10	1.44	0.17	0.42	-	0.410	2.49	18.56	1.89	18.17	1.85
S47	Parent	5	1.18	0.14	0.55	-	0.520	2.62	17.18	1.75	16.70	1.70
Average	Slumped		1.58	0.20	0.39	2.36	0.39	2.69	20.01	2.04	19.73	2.01
STDV	Parent		0.14	0.05	0.04	0.31	0.05	0.25	1.05	0.11	1.10	0.11
Average	Parent		1.60	0.17	0.41	0.81	0.39	2.70	19.90	2.03	19.50	1.99
STDV	Parent		0.23	0.03	0.07	0.19	0.07	0.24	1.74	0.18	1.75	0.18

Average	Total	1.59	0.19	0.40	1.74	0.39	2.69	19.97	2.04	19.65	2.00

IV. Soil samples 2016

GPS coordinates	Class	DBD [g *g^{-1}]	VMC [g *g^{-1}]	Porosity	KSAT [m^{-1} * d^{-1}]	Strength sample	Field Capacity [g *g^{-1}]	Specific gravity [g * cm^3]	Saturated Bulk weight [g * cm^3]	Bulk Weight at Field capacity [g * cm^3]
X71	Accumulated Material	1,64	0,34	0,50	-	-	0,42	3,28	21,02	20,25
X11	Accumulated Material	1,42	0,22	0,51	-	-	0,34	2,90	18,97	17,31
X14	Accumulated Material	1,43	0,25	0,55	-	-	0,43	3,18	19,40	18,19
X15	Accumulated Material	1,67	0,28	0,54	0,81	√	0,42	3,66	21,70	20,54
X41	Accumulated Material	1,46	0,33	0,54	12,92	√	0,44	3,19	19,65	18,63
X16	Accumulated Material	1,50	0,33	0,49	-	-	0,42	2,94	19,51	18,79
X17	Accumulated Material	1,71	0,29	0,50	-	-	0,40	3,41	21,69	20,68
X18	Accumulated Material	1,34	0,20	0,58	-	-	0,36	3,19	18,83	16,71
X19	Accumulated Material	1,42	0,37	0,58	-	-	0,46	3,36	19,62	18,44
X21	Accumulated Material	1,59	0,28	0,54	2,07	-	0,44	3,48	21,35	20,73
X22	Accumulated Material	1,59	0,41	0,52	0,39	-	0,46	3,31	20,68	20,11
X23	Accumulated Material	1,59	0,18	0,54	-	-	0,33	3,43	20,86	18,86
X24	Accumulated Material	1,47	0,33	0,61	3,36	-	0,43	3,75	20,39	18,65
X25(1)	Accumulated Material	1,55	0,30	0,51	0,52	√	0,41	3,17	20,20	19,22
X25 (2)	Accumulated Material	-	-	-	-	√		-	-	-
X26	Accumulated Material	1,65	0,28	0,57	1,17	√	0,40	3,84	21,79	20,17
X27	Accumulated Material	1,51	0,26	0,54	8,82	√	0,37	3,29	20,10	18,44
X28	Accumulated Material	1,46	0,27	0,53	0,59	-	0,30	3,12	19,51	17,25
X29	Accumulated Material	1,52	0,24	0,50	4,27	-	0,37	3,05	19,80	18,54
X1	Source Material	1,45	0,41	-	0,48	√		-	-	-

X2.2	Source Material	1,67	0,29	-	0,88	√		-	-	-
X2.1	Source Material	-	-	-	0,81	-		-	-	-
X3	Source Material	1,51	0,25	-	-	-		-	-	-
X4	Source Material	1,40	0,27	-	-	-		-	-	-
X5	Source Material	1,63	0,30	-	1,87	√		-	-	-
X6	Source Material	1,50	0,25	-	1,15	√		-	-	-
X7	Source Material	1,56	0,34	-	2,52	√		-	-	-
X8.1	Source Material	1,41	0,21	-	-	-		-	-	-
X8.2	Source Material	1,19	0,36	-	1,53	√		-	-	-
X9	Source Material	1,52	0,31	-	8,47	√		-	-	-
X10	Source Material	1,49	0,30	-	2,60	√		-	-	-
X2	Source Material	1,27	0,28	-	1,05	-		-	-	-
X12	Source Material	1,55	0,32	0,56	-	-	0,44	3,50	20,71	19,58
X13	Source Material	1,74	0,29	0,48	-	√	0,42	3,34	21,77	21,19
X91	Source Material	1,44	0,33	0,56	-	-	0,46	3,24	19,55	18,57
X31	Source Material	1,73	0,27	0,49	0,81	√	0,36	3,37	21,76	20,57
X21-1	Source Material	1,72	0,34	0,50	0,11	√	0,37	3,48	21,81	21,22
X20	Source Material	1,65	0,38	0,53	-	√	0,46	3,48	21,35	20,73
	Average	**1,53**	**0,30**	**0,53**	**2,60**		**0,41**	**3,33**	**20,50**	**19,31**